Tidally-Driven Intra-Seasonal Oscillations in the Thermosphere from TIEGCM-ICON and Connections to the Madden-Julian Oscillation

Federico Gasperini[1], Astrid Maute[2], Houjun Wang[1], Owen McClung[1], Deepali Aggarwal[3], and Komal Kumari[4]

[1]Orion Space Solutions
[2]CIRES/ University of Colorado Boulder
[3]Clemson University
[4]High Altitude Observatory

July 25, 2024

Abstract

Recent evidence has revealed that strong coupling between the lower atmosphere and the thermosphere ($>$100 km) occurs on intra-seasonal (IS) timescales ($\sim$30-90 days). The Madden-Julian Oscillation (MJO), a primary source of IS variability in tropical tropospheric convection and circulation, can influence the generation and propagation characteristics of atmospheric tides and has been proposed as a significant driver of thermospheric IS oscillations (ISOs). Despite this progress, the limited availability of satellite observations in the 'thermospheric gap' region (ca. 100-300 km) and the inability of numerical models to accurately characterize this region have hindered a comprehensive understanding of this connection and the fundamental processes involved. In this study, an Ionospheric Connection Explorer (ICON)-adapted version of the Thermosphere Ionosphere Electrodynamics General Circulation Model (TIEGCM), incorporating lower boundary tides derived from MIGHTI observations, is utilized to characterize and quantify the impact of the upward-propagating tidal spectrum on thermospheric ISOs and to elucidate connections to the MJO. Thermospheric zonal and diurnal mean zonal winds are shown to exhibit prominent ($\sim$20 m/s) tidally-driven ISOs throughout 2020-2021, largest at low latitudes ($\pm$30°) near $\sim$110-150 km altitude. Correlation analyses demonstrate a robust (r$>$0.6) connection between the thermospheric ISOs, tides, and the tropospheric MJO, moreover, Hovm\"oller diagrams indicate eastward tidal propagation consistent with the MJO and concurrent SABER observations. This study demonstrates that vertically propagating tides play a crucial role in linking IS variability from the lower atmosphere to the thermosphere, with the MJO identified as a primary contributor to this significant whole-atmosphere teleconnection.

Tidally-Driven Intra-Seasonal Oscillations in the Thermosphere from TIEGCM-ICON and Connections to the Madden-Julian Oscillation

Federico Gasperini[1], Astrid Maute[2], Houjun Wang[1], Owen McClung[1,3], Deepali Aggarwal[4], Komal Kumari[5]

[1]Orion Space Solutions, Louisville, CO, USA
[2]CIRES, University of Colorado, Boulder, CO, USA
[3]Ann and H.J. Smead Aerospace Engineering Sciences, University of Colorado, Boulder, CO, USA
[4]Department of Physics and Astronomy, Clemson University, Clemson, SC, USA
[5]High Altitude Observatory, National Center for Atmospheric Research, Boulder, CO, USA

Key Points:

- TIEGCM-ICON is used to quantify the impact of the upward-propagating tidal spectrum on thermospheric intra-seasonal oscillations (ISOs)
- Thermospheric mean zonal winds exhibit prominent (±20 m/s) tidally-driven ISOs largest at low latitudes near 110-150 km altitude
- Correlation and Hovmöller analyses demonstrate a strong connection with the tropospheric Madden-Julian Oscillation

Corresponding author: Federico Gasperini, `federico.gasperini@arcfield.com`

Abstract

Recent evidence has revealed that strong coupling between the lower atmosphere and the thermosphere (>100 km) occurs on intra-seasonal (IS) timescales (∼30-90 days). The Madden-Julian Oscillation (MJO), a primary source of IS variability in tropical tropospheric convection and circulation, can influence the generation and propagation characteristics of atmospheric tides and has been proposed as a significant driver of thermospheric IS oscillations (ISOs). Despite this progress, the limited availability of satellite observations in the 'thermospheric gap' region (ca. 100-300 km) and the inability of numerical models to accurately characterize this region have hindered a comprehensive understanding of this connection and the fundamental processes involved. In this study, an Ionospheric Connection Explorer (ICON)-adapted version of the Thermosphere Ionosphere Electrodynamics General Circulation Model (TIEGCM), incorporating lower boundary tides derived from Michelson Interferometer for Global High-resolution Thermospheric Imaging (MIGHTI) observations, is utilized to characterize and quantify the impact of the upward-propagating tidal spectrum on thermospheric ISOs and to elucidate connections to the MJO. Thermospheric zonal and diurnal mean zonal winds are shown to exhibit prominent (∼20 m/s) tidally-driven ISOs throughout 2020-2021, largest at low latitudes (±30°) near ∼110-150 km altitude. Correlation analyses demonstrate a robust (r>0.6) connection between the thermospheric ISOs, tides, and the tropospheric MJO, moreover, Hovmöller diagrams indicate eastward tidal propagation consistent with the MJO and concurrent Sounding of the Atmosphere using Broadband Emission Radiometry (SABER) observations. This study demonstrates that vertically propagating tides play a crucial role in linking IS variability from the lower atmosphere to the thermosphere, with the MJO identified as a primary contributor to this significant whole-atmosphere teleconnection.

Plain Language Summary

In recent decades, significant discoveries have highlighted how Earth's lower atmosphere, particularly tropical weather systems, can impact the thermosphere's dynamics. Of particular interest are solar tides generated by deep convection in the tropics that propagate upward into the thermosphere. The Madden-Julian Oscillation (MJO), a periodic weather phenomenon, influences these upward-propagating tides. Advances in satellite technology have allowed scientists to observe and quantify these effects more accurately.

In this study, we used a numerical model of the ionosphere-thermosphere (TIEGCM), incorporating lower boundary tides from the Ionospheric Connection Explorer (ICON) satellite mission, to examine the connection between solar tides, intra-seasonal oscillations (ISOs) in the thermosphere, and the tropospheric MJO. Results show that near the equator in the thermosphere, at altitudes of 110-150 km, average east-west winds exhibit significant ISO variations driven by tides, reaching amplitudes of more than 20 m/s. These variations are strongly correlated with changes in upward-propagating diurnal tidal amplitudes, whose longitude-time variation is consistent with the MJO and independent Sounding of the Atmosphere using Broadband Emission Radiometry (SABER) satellite observations. This study underscores the pivotal role of upward-propagating solar tides in connecting ISOs from the lower atmosphere to the thermosphere, highlighting the Madden-Julian Oscillation (MJO) as the primary driver of this connection.

1 Introduction

The structure and dynamics of the thermosphere, spanning altitudes of approximately 100-500 km, are influenced by external processes associated with the Sun and magnetosphere (e.g., Thayer and Semeter, 2004; Johnson and Heelis, 2005), as well as internal processes related to atmospheric waves propagating from the lower atmosphere (Andrews et al., 1987). These waves are characterized by different spatiotemporal scales and include global-scale solar tides, planetary waves, and Kelvin waves, as well as smaller-scale gravity waves (e.g., Fritts and Alexander, 2003; Forbes et al., 2009; Pancheva et al., 2012; Gasperini et al., 2015; Yiğit and Medvedev, 2015; Liu et al., 2016). Of particular interest in understanding the thermosphere's dynamics, known to vary significantly from intra-seasonal (IS) to inter-annual time scales (e.g., Sassi et al., 2019), is the role of upward-propagating solar tides (e.g., Gasperini and Oberheide, 2024 and references therein). Emerging modeling and space-based evidence suggest that much of the IS variability of the thermosphere is connected with an IS-modulated vertically propagating tidal spectrum (e.g., Li and Lu, 2020, 2021; Yang et al., 2018; Vergados et al., 2018; Gasperini et al., 2017, 2020; Kumari et al., 2020, 2021).

Solar tides are persistent and ubiquitous global-scale oscillations observed in various atmospheric fields, such as wind, temperature, pressure, density, and geopotential height, with periods that are integer fractions of a solar day (Chapman and Lindzen, 1970; Matsushita 1967a,b; Forbes 1995; Hagan et al., 1995). The notation DWs or DEs is used to describe westward or eastward-propagating diurnal tides, respectively, with zonal wavenumber 's'. For semidiurnal tides, 'S' replaces 'D', while zonally symmetric oscillations are denoted as D0 and S0. Solar tides can be excited through several mechanisms, including the absorption of solar radiation, large-scale latent heat release from deep convective clouds in the troposphere, the gravitational pull of the Sun, and secondary waves resulting from nonlinear wave-wave interactions (Palo et al., 1999; Chang et al., 2011; Liu, 2016; Gasperini et al., 2015, 2021, 2022; Forbes et al., 2021a,b; Gasperini and Oberheide, 2024).

The Madden-Julian Oscillation (MJO) (Madden and Julian, 1971, 1994) represents the principal mode of IS variability in tropical convection and circulation and has been a focus of extensive research since its discovery due to its critical role in medium-range weather forecasting. Characterized as an eastward-moving disturbance within low latitudes ($\pm 30°$), the MJO typically recurs every 30-90 days, influencing tropical winds, clouds, rainfall, and numerous other atmospheric variables (Zhang, 2005). The Real-time Multivariate MJO series 1 (RMM1) and 2 (RMM2) indices (Wheeler and Hendon, 2004) are commonly utilized to identify the MJO. This oscillation generates a spectrum of global-scale waves, predominantly through convective forcing (Wheeler and Kiladis, 1999), and exhibits significant dependence on seasonal variation, MJO magnitude, and phase. Despite the rapid attenuation of the MJO above the tropopause due to its low frequency and slow zonal propagation speed (e.g., Zhang, 2005; Tian et al., 2012), its impacts have been observed in lower thermospheric gravity waves (e.g., Karoly et al., 1996; Eckermann et al., 1997; Moss et al. 2016; Li and Lu, 2020, 2021) and solar tides (e.g., Yang et al., 2018; Vergados et al., 2018; Gasperini et al., 2017, 2020; Kumari et al., 2020, 2021). Early investigations into MJO signals within the lower thermosphere were limited and predominantly based on radar wind observations. Eckermann et al. (1997) and Lieberman (1998) suggested that while the MJO is confined to the lower atmosphere, it could modulate upward propagating tides and gravity waves, potentially inducing similar periodic signatures across various vertical levels. Subsequently, Lieberman et al. (2007) proposed that this whole atmosphere IS coupling involving tidal variability can occur through several mechanisms: variability in tropospheric heating that generates the tides; interactions with the zonal mean flow, which modulate tidal behavior as waves propagate through a variable background in the middle and upper atmosphere; or nonlinear wave-wave interactions.

As noted above, the influence of the MJO on tides and the related effects on the thermosphere was first suggested over two decades ago. However, only recent advancements in satellite observational capabilities and physics-based models have enabled improved quantification and characterization of these effects. Satellite-based thermospheric observations (e.g., Gasperini et al., 2017, 2020; Kumari et al., 2020) and modeling efforts (e.g., Yang et al., 2018; Vergados et al., 2018; Gasperini et al., 2020; Kumari et al., 2021) have demonstrated a robust connection between solar tides in the thermosphere and the tropospheric MJO. Using cross-track wind measurements from the Challenging Minisatellite Payload (CHAMP) and the Gravity field and steady-state Ocean Circulation Explorer (GOCE) satellites, along with high-resolution Thermosphere-Ionosphere-Mesosphere-Electrodynamics General Circulation Model (TIME-GCM) simulations forced with Modern-Era Retrospective Analysis for Research and Applications (MERRA) reanalysis data, and Outgoing Longwave Radiation (OLR) data, Gasperini et al. (2017) identified significant 90-day oscillations in thermospheric zonal mean and DE3 zonal winds during 2009-2010, linking these oscillations to variability in tropospheric convective activity. Following this study, Vergados et al. (2018) used 14 years of Sounding of the Atmosphere using Broadband Emission Radiometry (SABER) temperature measurements to show distinct IS oscillations (ISO) in the low-latitude lower thermosphere and connections to tides. Kumari et al. (2020) showed that the MJO influences the DE3 and DW1 temperature tides in the lower thermosphere by $\sim$25% and $\sim$10% (peak-to-peak), respectively. Their findings indicated a strong seasonal dependency of the MJO influence, with Kumari et al. (2020) observing robust effects across all seasons, dependent on the MJO phase and location. Moreover, they observed that the seasonal variations in the IS variability of nonmigrating tides at various MJO locations were found to be more pronounced than those in migrating diurnal tides. Further investigation by Kumari et al. (2021), using Specified-Dynamics Whole Atmosphere Community Climate Model with thermosphere and ionosphere extension (SD/WACCM-X), found that IS variability in tidal heating plays a more crucial role than tidal amplitude modulation by background winds in imprinting the MJO signal on low-latitude lower thermospheric tides. The MJO modulation of tides (and ultra-fast Kelvin waves, not discussed here), extends well into the thermosphere, as evidenced by in-situ wind observations near 260 km from the GOCE satellite (Gasperini et al., 2020) and there is observational evidence of MJO modulation of thermospheric zonal and diurnal mean winds (∼20 m/s peak-to-peak) from CHAMP and GOCE satellite diagnostics (Gasperini et al., 2017).

These recent studies highlight significant coupling between the troposphere and thermosphere on IS timescales, prompting critical questions with broad implications for the entire atmospheric system. Understanding the connection between the MJO and the upward-propagating tidal spectrum, and the impact of the MJO-modulated wave spectrum on the thermosphere, is a crucial next step for improving whole atmosphere prediction capabilities. Further investigation of the IS variability of the thermosphere and connections to the MJO is thus warranted. In light of these considerations, two major goals addressed by this study are (1) to better understand the role that tidal variability from the lower and middle atmosphere play in producing thermospheric zonal wind ISOs, and (2) to examine connections between thermospheric winds, tidal variability, and the tropospheric MJO. These advancements are crucial to achieving an improved understanding of the coupling between terrestrial weather and variability in the 'entangled' thermosphere-ionosphere (T-I) system.

This paper is structured as follows: Section 2 introduces the data and model used; Section 3 contains a brief description of the methods and techniques employed; Section 4 presents the results; and Section 5 summarizes the main conclusions of the study.

2 Data and Model

2.1 OLR

The daily Outgoing Longwave Radiation (OLR) Climate Data Record (CDR) quantifies the amount of infrared radiation emitted from the Earth's surface and lower atmosphere into space, providing insights into cloud cover and water vapor distribution (Gruber and Winston, 1978). Since 1979, this record has primarily utilized data from high-resolution infrared radiation sounders, supplemented by newer technologies such as the Infrared Atmospheric Sounding Interferometer (IASI) since 2007 and the Cross-track Infrared Sounder (CrIS) since 2012. To enhance accuracy, OLR data is also derived from operational geostationary imagers, integrating multiple sources through statistical methods like OLR regression, prediction coefficients for instrument temperature, and corrections for inter-satellite biases. The dataset to be used for this study consists of daily OLR values binned in a 2.5° latitude x 2.5° longitude global grid with gaps that are temporally and spatially interpolated (Liebmann and Smith, 1996). OLR estimation algorithms have an accuracy of about 4-8 Wm^{-2} (Kayano et al., 1995).

2.2 RMM MJO index

The Real-time Multivariate MJO (RMM) index is utilized to monitor the MJO. MJO events are commonly identified using RMM series 1 (RMM1) and series 2 (RMM2), as detailed in Wheeler and Hendon (2004). The RMM index identifies the strength and position of the MJO's active phase, characterized by extensive and persistent cloudiness typically observed in the Indian Ocean region. Comprising the first two principal components (PCs) derived from OLR, 850-hPa zonal wind, and 200-hPa zonal wind averaged between 15° S and 15° N, the RMM index provides a quantitative measure of the MJO's intensity and location within the tropics. MJO events are grouped into eight active phases (Phases 1-8) according to the amplitude and phase information obtained by combining the RMM1 and RMM2 values, with enhanced convection moving eastward from the central Pacific to the Indian Ocean. An 'active' MJO event is said to occur when an RMM index is greater than 1 for at least 5 consecutive days. This study presents correlative findings utilizing RMM1 as a proxy for MJO variability, given its highest correlation with thermospheric parameters. Notably, similar conclusions can be derived when using MJO amplitude or RMM2. Investigating the underlying causes for the stronger correlations observed with RMM1, as opposed to RMM2 and MJO amplitude, is beyond the scope of this work.

2.3 ICON/MIGHTI

NASA's Ionospheric Connection (ICON) Explorer is a Heliophysics System Observatory (HSO) mission with the primary objective to observe how the ionosphere is influenced by the dynamics of the neutral atmosphere (Immel et al., 2018, 2021; Immel and Eastes, 2019). ICON was launched on 10 October 2019 on a nearly circular ∼27° inclination orbit near 590 km altitude, providing concurrent measurements of the thermospheric and ionospheric environments through 10 November 2022. Operating as a single observatory, ICON collected data covering two local solar times (LST) per day at a particular latitude, each progressing approximately 29.8 minutes earlier daily. ICON's Michelson Interferometer for Global High-resolution Thermospheric Imaging (MIGHTI) instrument provides day and night vector winds with a precision of ∼8.7 m/s (Harding et al., 2021, 2023) and temperatures with uncertainty of around 7 K (Stevens, 2022) in the ∼94-105 km altitude region.

2.4 TIMED/SABER

The Thermosphere Ionosphere Mesosphere Energetics Dynamics (TIMED) satellite was launched in December 2001 into a circular orbit near 625 km altitude with a ∼74° inclination (Russell et al., 1999). Sounding of the Atmosphere using Broadband Emission Radiometry (SABER) is a limb-scanning infrared radiometer onboard TIMED, operating with 10 broadband channels spanning 1.27-17 μm. SABER retrieves kinetic temperatures from CO_2 emissions at 15 μm and 4.3 μm wavelengths, covering altitudes from roughly 20-120 km (Mertens et al., 2001). The retrieval errors are ±1-2 K below ∼70 km, with an additional error of ∼1.4 K at higher altitudes due to nonlocal thermodynamic equilibrium (non-LTE) effects (Remsberg et al., 2008). Here, we will utilize SABER temperature data (v2.0 Level 2). This data set provides global coverage in one day and captures two different local times (LTs) for any given latitude.

2.5 TIEGCM-ICON

The Thermosphere-Ionosphere-Electrodynamics General Circulation Model (TIEGCM) developed by the National Center for Atmospheric Research (NCAR)'s High-Altitude Observatory (HAO), is a first-principle, time-dependent, three-dimensional self-consistent numerical model of the thermosphere (Dickinson et al., 1984; Roble et al., 1988; Richmond et al., 1992; Qian et al., 2014, 2024), which includes the dynamics, energetics and chemistry with a steady-state ionospheric electrodynamo in a realistic geomagnetic main field defined by the International Geomagnetic Reference Field (IGRF-13) (Alken et al., 2021). The initial developments of the TIEGCM can be traced back to seminal works by Dickinson et al. (1984), Roble et al. (1988), and Richmond et al. (1992). Recent advancements are documented in studies such as Qian et al. (2014), Richmond and Maute (2013), Qian et al. (2024), and related references. TIEGCM v2.0 covers altitudes ranging from approximately 97 km up to 450-600 km, with 'standard' resolution set at 2.5° by 2.5° in geographic longitude and latitude, and four grid points per scale height vertically. The ionospheric electrodynamics are computed within a modified magnetic apex coordinate system (Richmond, 1995), while the solar spectral fluxes are determined by the Extreme Ultra-Violet (EUV) flux model for aeronomic calculations (EUVAC) model

(Richards et al., 1994), utilizing observed F10.7 values. Simulations are conducted with a timestep size of 30 seconds, and helium is considered a major species (Sutton et al., 2015). Ion convection patterns, as described by the Weimer (2005) model, are driven by 5-min Interplanetary Magnetic Field (IMF) 'By' and 'Bz' magnitudes, along with solar wind velocity and density. High latitude energy input associated with auroral particle precipitation is modeled based on an analytical auroral model (Roble and Ridley 1987).

An ICON-adapted version of TIEGCM (Maute 2017; Maute et al., 2023), herein referred to as 'TIEGCM-ICON', is employed. In this TIEGCM-ICON configuration, the model's lower boundary (LB) is specified based on ICON/MIGHTI wind and temperature measurements using an HME fitting method (e.g., Forbes and Hagan 1982; Oberheide et al. 2011a,b). As mentioned in Section 2.3, MIGHTI provides wind and temperature data over both day and night in the lower thermosphere (ca. 94-105 km). Over a 24-hour LST cycle of around 41 days, these wind and temperature data sample every combination of longitude and LST extending from about 10°S to 40°N latitude. These data are used to derive global fits to empirical HME functions. These fits provide an estimate of the global structure of the upward propagating diurnal and semidiurnal tides in the lower thermosphere. Further details on the HME fits for ICON can be found in Forbes et al. (2017) and Cullens et al. (2020). TIEGCM-ICON is based on the TIEGCM v2.0 release with descriptions of the model by Qian et al. (2014). A description of the TIEGCM-ICON and the differences to TIEGCM v2.0 is provided in Section 2.2 of Maute (2017). Tidal propagation is notably influenced by the atmospheric background; hence, employing a realistic background improves the characterization of seasonal and latitudinal variability in tidal propagation and dissipation (e.g., Jones et al., 2014). TIEGCM-ICON incorporates background climatologies from the Mass Spectrometer Incoherent Scatter Radar Extended (MSISE00) (Picone et al. 2002) and the horizontal wind model (HWM07). Based on Jones et al. (2014), no significant differences are expected by replacing HWM07 with HWM14 (Drob et al. 2015). It should be noted that, given the focus on IS time scales, no significant impacts are expected on the results contained in Section 3 from the particular background climatologies selected for running TIEGCM-ICON.

This study employs three TIEGCM-ICON simulations for analysis, all extending from December 2019 to January 2022:

- **Run 1:** HME diurnal/semidiurnal tidal forcing at the LB, realistic geophysical forcing (*'WeiHmeV2'*)
- **Run 2:** HME diurnal/semidiurnal tidal forcing at the LB, constant geophysical forcing (*'WeiHmeV2_conGeop'*)
- **Run 3:** no tidal forcing at the LB, realistic geophysical forcing (*'WeiNoHmeV2'*)

3 Methods

Various methodologies are used to isolate the IS variability in the TIEGCM-ICON thermospheric winds and tides, and to investigate their connections to tropospheric sources. Analyses are concentrated on latitudes ±60°, where the tidal coupling between the lower/middle atmosphere and the thermosphere is most effective. The statistical significance of spectral peaks is established through wavelet-type analysis, a technique commonly used to analyze localized variations of power within a time series (Torrence and Compo, 1998). This approach allows the decomposition of a time series into time-frequency space, enabling the identification of dominant modes of variability and their temporal evolution. Wavelet transforms have been widely applied in geophysical studies, including those on tropical convection and thermosphere-ionosphere (T-I) interactions (Yamazaki, 2023). In this study, we utilize the wavelet analysis package of Torrence and Compo (1998), incorporating the rectification method of Liu et al. (2007) to enhance accuracy and reliability.

The analyses are performed on 'filtered' time series to isolate IS variations in the relevant quantities within the time domain and to gain insights into their amplitudes and temporal variability. This 'filtering' process involves: (a) creating residuals for each day by subtracting 90-day running means from the raw data; and (b) applying a 5-day running mean to the residuals to reduce noise. While this 'filtering' is not a 'true' band-pass filter, it has been successfully employed to study periodic signals in thermospheric data in the time domain (e.g., Forbes et al., 2006; Hughes et al., 2022; Gasperini et al., 2023). In this study, we refer to these 5-day running means of 90-day residuals as 'filtered' time series. Furthermore, correlation analyses are used to identify and characterize IS variations in the thermosphere and their potential tropospheric sources. Specifically, lagged correlation analysis is performed on (a) the time series of MJO RMM1 index and thermospheric tides, and (b) the time series of thermospheric tides and the ISO amplitude of the zonal mean zonal wind. Correlation coefficients are determined using Pearson's distribution, with thermospheric oscillations treated as the independent variable and tropospheric oscillations as the dependent variable. A moving correlation coefficient, as described at the end of Section 4, is utilized to provide further insights.

Characterizing the complete diurnal and semidiurnal tidal spectrum necessitates resolving zonal wavenumbers and periods (e.g., Yamazaki 2023). This analysis requires two-dimensional (2-D) spatiotemporal data, specifically data as a function of longitude and time. Techniques such as the 2-D fast Fourier transform (FFT) (e.g., Hayashi, 1971) and the 2-D least squares fitting method (e.g., Wu et al., 1995) can be employed to determine the zonal wavenumber, wave period, amplitudes, and phases of a particular tidal component. Given the transient nature of tides in the lower thermosphere, a short-time analysis is typically utilized. In this study, for tidal analysis of the TIEGCM-ICON model output, we apply the 2D (space-time) FFT on a daily basis, progressing one day at a time. The spectral decomposition technique of Hayashi (1971) is used to resolve westward or eastward propagating waves. The Hayashi (1971) method is straightforward to implement, and its spectrum directly provides wave amplitudes in units of the input data, facilitating interpretation. It is important to note that while the TIEGCM-ICON lower boundary (LB) tides are derived using 41-day means of ICON MIGHTI observations, the effects of dissipation and mean winds above the LB, nonlinear interactions, and in situ wave generation can cause significant day-to-day variability in the thermospheric tidal spectrum. Thus, TIEGCM tidal amplitudes and phases are obtained on a daily basis using the technique discussed above.

Additionally, to examine the connection between the MJO and tidal variations, we employ a standard MJO diagnostic known as Hovmöller analysis (Wheeler & Kiladis, 1999), following an approach similar to Kumari et al. (2021). The Hovmöller analysis involves: (a) applying a 30-90 day bandpass filter on tidal amplitudes and phases and (b) extracting the eastward-propagating signal. Unlike previous studies (e.g., Gasperini et al., 2020; Kumari et al., 2020; Yang et al., 2018), which focused solely on tidal amplitudes, the analysis incorporates tidal phase values into the Hovmöller analysis of tidal perturbations. As noted by Kumari et al. (2021), this bandpass filtering reduces noise errors in the input data thus resulting in a 'cleaner' MJO signature.

4 Results

The focus of this study is on the period spanning from 1 January 2020 to 31 December 2021, characterized by low geomagnetic and solar activity influences. Initially, we assess the geophysical conditions specific to this timeframe. Figure 1 includes time series plots of daily Kp geomagnetic and F10.7 solar radio flux indices (black lines), alongside their filtered counterparts (blue lines) and wavelet analyses of their daily filtered values. Daily Kp values consistently remain below 3.0, indicative of (relatively) low geomagnetic activity conditions. The F10.7 solar flux shows variability within the range of 75 SFU to 125 SFU, typical for solar minimum to medium conditions. Filtered Kp (F10.7) values range from -1 (-20 SFU) to +2 (+20 SFU). Wavelet analyses of Kp and F10.7 reveal pronounced variations with periods close to the solar rotation period of ∼27 days, particularly notable during September-December 2020 and July-December 2021, as corroborated by the filtered time series. Additionally, Figure 1 depicts the time series of OLR and RMM1 indices (black lines), along with their filtered time series (blue lines) and wavelets. In contrast to the geomagnetic and solar indices, which exhibit significant variations in the 20-40 day range, OLR and RMM1 demonstrate prominent IS variations spanning periods from 40 to 120 days throughout the two years. These IS variations in RMM1 will be further analyzed in subsequent sections of this study.

Next, we analyze the near-equatorial (±15° average) zonal- and diurnal-mean (i.e., longitudinal and 24-hour UT/LT averaged, hereafter 'ZDM') zonal winds at ∼150 km (pressure level 20) and ∼300 km (pressure level 40) altitudes for the three TIEGCM-ICON cases listed in Section 2.5: ('Run 1') TIEGCM with HME tidal forcing at the LB and realistic geophysical forcing ('WeiHmeV2'), ('Run 2') TIEGCM with HME tidal forcing at the LB but constant geophysical forcing ('WeiHmeV2_conGeop'), and ('Run 3') TIEGCM with no tidal forcing at the LB but with realistic geophysical forcing ('WeiWoHmeV2r1'). Geophysical forcing for 'Run 2' is: F10.7=71 sfu, solar wind speed = 400km/s; solar wind density = 4.1/cm^3, IMF By=0 nt, Bz=1nT, hemispheric power = 12 GW. The time series of ZDM zonal winds at ∼150 km altitude for 'Run 1', 'Run 2', and 'Run 3' are depicted in Figures 2a_1-2c_1, respectively, showing daily values (black lines) and filtered values (blue lines), while their corresponding Morelet wavelets are presented in Figures 2a_2-2c_2. For 'Run 1', the time series and wavelets reveal significant IS variability of about ±15 m/s over the span of 2 years, exhibiting a particularly pronounced periodicity of around 64 days. This periodic behavior in the ZDM zonal winds, peaking notably around October-

December 2020 and July-November 2021, mirrors similar periodicities observed in OLR and RMM1 (ref. Figures $1c_2$ and $1d_2$). Note that the influence of the MJO on the thermosphere is distinct from the differences observed between years of equinox transition. While both phenomena can impact atmospheric dynamics, the MJO's influence is related to its IS variability and the propagation of its associated atmospheric waves. In contrast, the differences between years of equinox transition are mainly driven by annual changes in solar radiation and the resulting variations in atmospheric circulation patterns. Therefore, these influences are not the same but may interact in complex ways to affect thermospheric conditions. Additionally, variations of about ± 5 m/s occurring near 27 days (and its harmonics at $\sim$13.5 days and $\sim$54 days), evident during August 2020, April-May 2021, and October-November 2021, are closely aligned with variations in the geomagnetic (Figure $1a_2$) and solar (Figure $1b_2$) indices. These fluctuations are attributed to the well-documented influence of solar rotation variation in EUV flux on thermospheric parameters (e.g., Qian and Solomon, 2012 and references therein). In contrast, 'Run 2' displays substantial IS variability akin to 'Run 1', but lacks the characteristic variability around 27 days associated with solar and geomagnetic activity as geophysical forcing is kept constant for this case. Similarly, a direct comparison of unfiltered ZDM zonal wind time series between 'Run 1' and 'Run 2' clearly highlights shorter-term ($\sim$5-30-day) solar/geomagnetic-induced variations in 'Run 1', absent in 'Run 2'. The observed differences are anticipated, considering the lack of variability in external geophysical forcing for 'Run 2'.

A compelling result is obtained from the analysis of 'Run 3'. The time series (Figure $2c_1$) and wavelet (Figure $2c_2$) of 'Run 3' reveal solar/geomagnetic-induced variations around 27 days and their harmonics, but lack any IS variations in the 60-100 day range, notably the $\sim$64-day variation observed in both 'Run 1' and 'Run 2'. This finding indicates that the ± 15 m/s variability in ZDM zonal winds around 150 km in 'Run 1' and 'Run 2' is largely driven by the diurnal and semidiurnal tides propagating from below $\sim$97 km. Although these results specifically address the 150 km altitude region, similar conclusions apply to higher altitudes, such as near 300 km, as illustrated in Figures $2d_1 - f_1$ and $2d_2 - f_2$. Detailed analyses of latitudinal and altitudinal dependencies in the IS response of ZDM winds to the upward propagating tidal spectrum are provided in subsequent sections.

The results presented in Figure 2 demonstrated that the diurnal/semidiurnal tidal spectrum entering the lower thermosphere near 97 km is a leading driver of the dynamical variability in the mean thermospheric zonal winds around IS time scales. Comparable results have been observed for other model parameters, such as thermospheric temperature, composition, and density. It is likely that ionospheric quantities, including electron density, ion drifts, and total electron content, will exhibit similar effects, which will be investigated in a dedicated follow-up study. Next, we aim to characterize the altitude, latitude, and month-of-year (moy) dependencies on this tidal-induced IS variability in ZDM zonal winds. To this end, we compute difference fields between the full model outputs from 'Run 1' (with ICON/HME tides at the LB) and 'Run 3' (with no tides at the LB). Note that both 'Run 1' and 'Run 3' incorporate the same geophysical forcing, hence the difference fields are expected to exhibit negligible variability associated with 'external' forcing and thus enable us to focus on the thermospheric effects from the LB tides.

Next, we examine the altitude-moy contours of the ZDM zonal winds near the equator (±15°) from 'Run 1' (Figures $3a_1$) and the 'Run 1' - 'Run 3' difference field (Figures $3a_2$), along with the 5-90-day-filtered variations of the difference field (panel a_3). Consistently with the wavelet results in Figure 2, the IS variations in ZDM zonal winds maximize around October-December 2020 and July-November 2021 with variability up to ±20 m/s. The altitude-moy structure of the filtered ZDM winds is in general agreement with previous modeling results by Gasperini et al. (2017) who examined a MERRA-2-forced TIMEGCM simulation and satellite observation during 2009-2010 demonstrating a connection between the background zonal winds, the DE3 tide, and tropical tropospheric convection. Using only a model simulation with realistic lower boundary and external forcing, Gasperini et al. (2017) could not unequivocally determine and quantify the sources of IS variations in the mean winds and the associated dependencies on altitude and latitude. As shown in Figure $3a_3$, the tidally-induced zonal wind ISOs maximize in the lower thermosphere near 110-130 km altitude. This region is where upward-propagating tidal components undergo significant dissipation imparting their energy, momentum, and temporal variability to the background (e.g., Truskowski et al., 2014). Remarkably, and in agreement with Gasperini et al. (2017), the tidally-driven mean wind ISOs retain significant values even in the middle and upper thermosphere with variations exceeding ±15 m/s near 400 km altitude.

Proceeding further, we investigate the tidally-induced latitude-moy structure in the ZDM zonal winds around two altitudes of interest: 150 km (Figures $3b_1-b_3$) and 300 km (Figures $3c_1-c_3$). For both altitudes, the IS variability is shown to be most prominent within about ±20° latitude (ref. Figures $3b_3$ and c_3) and display values up to about ±20 m/s (±15) near 150 km (300 km). Notably, the latitude structure of the ISOs is strongly seasonally-dependent. A closer examination of Figures $3a_3$ and $3b_3$ reveals dominant equatorially symmetric and asymmetric latitude structures that vary in importance through the two years. This result points to the collective effect of multiple tidal components in determining the latitude-moy-altitude structure of the background zonal wind. Each tidal component has its dominant Hough modes, with the amplitude of each Hough mode strongly dependent on latitude and season (e.g., Oberheide et al., 2011a,b; Forbes et al., 2022; Gasperini and Oberheide, 2024). The effect of different tidal components on the observed zonal wind ISOs is examined in further detail in the later part of this study. Note that due to the ∼41-day averaging associated with the MIGHTI/HME fitting, tidally-driven ZDM zonal winds exhibit no appreciable variability with periods shorter than ∼30 days. Consequently, it is deemed appropriate to employ 5-90 day 'filtered' fields (as detailed in Section 3) to quantify 'IS variability'.

Figure 4 investigates the altitude-latitude structure of IS variations induced by tides in the ZDM zonal winds, focusing on two specific days with significant and oppositely-phased IS variations: 10 October 2020 (Figures $1a_1$-$1a_3$) and 10 November 2020 (Figures $1b_1$-$1b_3$). Similar to Figure 3, the ZDM zonal winds in Figure 4 are derived from the difference field between 'Run 1' and 'Run 3'. Furthermore, filtering is applied to this mean zonal wind field to highlight IS variations. The IS variability is found to be in the ±10-15 m/s range, with increased westward (eastward) ZDM zonal winds between approximately 10°S-20°N and 60°S-40°S (40°S-10°S and 20°N-60°S) on 10 October. A nearly opposite latitudinal response is observed on 10 November, with increased eastward winds around ±20-30° latitude and westward wind enhancements generally present at mid-latitudes. A more detailed visual inspection of Figure 4 reveals significant latitudinal asymmetries in the background zonal wind response to the upward propagating tidal spectrum. The winds are shifted toward the northern hemisphere by about 10° on both 10 October and 10 November, likely due to the effect of mean wind. Vertically varying mean winds can effectively alter the altitude-latitude propagation characteristics of different tidal modes, strongly depending on the longitudinal direction of propagation, frequency, and wavenumber. More discussion on this topic is provided below as the latitude-moy structure and IS variability of different tidal components are examined. Finally, as best exemplified in Figures $4a_3$ and $4b_3$, it is important to note that the altitude of maximum background wind variations occurs around 100-130 km, the altitude region where the upward-propagating tidal spectrum capable of reaching the lower thermosphere undergoes the most significant dissipation. Variability in the dominant tidal components is likely to be a leading source of difference in the altitude-latitude structures between the two days.

The ICON-HME-informed TIEGCM simulations have thus far demonstrated the prominent role of the lower thermospheric diurnal and semi-diurnal tidal spectrum in generating IS variability in the ~100-400 km altitude region, with the strongest effects on the background zonal wind occurring at low latitudes and around 110-130 km altitude. Next, to gain better insights into the role played by the upward-propagating tidal spectrum we analyze the altitude-moy and latitude-moy structures of the nonmigrating DE2 and DE3 tides and the migrating DW1 and SW2 tides. It is important to note that, aside from DE2 and DE3, other upward-propagating tidal components from the lower/middle atmosphere can play an important role in the whole-atmosphere coupling on IS timescales (notably SE2 and DE1). However, it would be beyond the scope of this paper to examine all the tidal components from these model simulations in detail and this effort is left for follow-on work that may need to account also for terdiurnal tides and ultra-fast Kelvin waves. The vertical structure of zonal wind DE2, DE3, DW1, and SW2 amplitudes as a function of time (2020-2021) between 100 km and 400 km from TIEGCM-ICON 'Run 1' are contained in Figures $5a_1$-$5d_1$, respectively. Figures $5a_1$-$5d_1$ present the unfiltered tidal amplitudes, while Figures $5a_2$-$5d_2$ display the same components after the application of a 5-90-day filter to highlight IS variability. From these depictions, it is clear that the amplitudes of the nonmigrating DE2 and DE3 tides grow exponentially with height up to ~120 km, the altitude region where dissipation stops their growth causing the amplitudes to decrease before reaching asymptotic values above about 200 km altitude. Molecular diffusion is the dominant dissipation mechanism for vertically propagating waves in the thermosphere.

As established by Chapman and Lindzen (1970), the exponential growth of an upward-propagating tide ceases in altitude regions where the timescale for molecular dissipation approximates the wave period ($\chi \sim 1$). In this context, χ is defined as $\chi = \left| \frac{2\pi}{\lambda_z^2} \frac{\mu_0}{\rho} \frac{1}{\sigma} \right|$, where λ_z represents the vertical wavelength, μ_0 denotes the molecular dissipation coefficient,

ρ is the mean density, and σ stands for the wave frequency. When $\chi \sim 1$, molecular processes dominate, and a tide shifts from exponential growth to decay. The altitude where $\chi \sim 1$ depends quadratically on λ_z^2, and also varies with the wave frequency σ and mean density ρ. The first symmetric Hough modes of DE2 and DE3 encounter $\chi \sim 1$ in the altitude range of approximately 110-130 km, corresponding to peaks in amplitude as shown in Figures $5a_1$-$5b_1$. As previously mentioned, classical tidal Hough functions serve as the orthogonal bases for the latitudinal structure of tidal components, while HMEs represent the altitude extension of these Hough functions incorporating tidal dissipation mechanisms. Tides can be expressed as a combination of HMEs. The primary characteristics of the DE3 in the MLT can be effectively captured by a combination of the first symmetric mode (equatorial, HME1) and the first antisymmetric mode (non-equatorial, HME2), whereas DW1 is predominantly composed of the first symmetric component (HME1). The symmetric DW1 mode is largely driven by tropospheric heating, while the two main modes in DE3 result from both tropospheric heating and mean zonal wind variations in the stratosphere and lower mesosphere. DE3 generally exhibits its strongest amplitudes from July to November, with peak amplitudes around 15 m/s in zonal winds near 95 km (e.g., Talaat and Lieberman, 1999; Forbes et al., 2003) and upward of 20 m/s near 260 km (e.g., Gasperini et al., 2015, 2020).

As a major driver of IS variability in the thermosphere, DE3 originates from latent heat release in deep convective clouds in the tropical troposphere (e.g., Hagan et al., 1997; Hagan and Forbes, 2002; Oberheide et al., 2011a,b). The symmetric mode HME1 of DE3, characterized by λ_z of ~56 km, extends higher into the thermosphere and peaks typically from July to November (e.g., Oberheide et al., 2011a,b; Forbes et al., 2022; Gasperini et al., 2023, 2024). Conversely, the antisymmetric mode HME2 of DE3, with λ_z ~30 km, shows increased amplitudes, dominating the DE3 spectrum from December to February. Mean wind fields are known to significantly distort the altitude-latitude tidal structures between 100 and 400 km (Gasperini et al., 2017). The asymmetries in DE3 and other upward-propagating tidal components primarily arise from the linear superposition of one or more antisymmetric modes, generated through processes such as 'mode coupling' (e.g., Lindzen and Hong, 1974) or 'cross-coupling' (e.g., Walterscheid and Venkateswaran, 1979a, 1979b). Mean winds primarily distort the height-latitude structures of eastward propagating waves, like DE3 and DE2, by aligning them with westward wind regimes in the thermosphere. Theoretical interpretations (e.g., Forbes and Vincent, 1989; Forbes, 2000; Gasperini et al., 2017) suggest that westward (eastward) zonal mean winds Doppler-shift eastward propagating waves to higher (lower) frequencies and longer (shorter) vertical wavelengths, thus reducing their dissipation effects.

The unfiltered DE2 (Figure $5a_1$) shows prominent maxima below 200 km and significant amplitudes extending up to 300 km, with clear periodic enhancements occurring approximately every few months. The filtered DE2 amplitudes (Figure $5a_2$) highlight large IS variations, with the most significant activity around 100-150 km and recurring peaks indicating variability of around 10-30 days. The DE3 tidal component (Figure $5b_1$) displays strong seasonal maxima around 150 km, with amplitudes decreasing with altitude. The filtered DE3 (Figure $5b_2$) reveals pronounced IS variability, particularly notable around 100-150 km, exhibiting periodic fluctuations over 5-60 days. The DW1 component (Figure $5c_1$) exhibits comparatively much smaller IS amplitudes of around ± 6 m/s (versus $\sim$80 m/s maximum amplitudes), likely due to the upward-propagating component and nonlinear wave-wave interactions. The unfiltered SW2 (Figure $5d_1$) shows distinct seasonal peaks around 150 km, with amplitudes extending above 200 km. The filtered SW2 (Figure $5d_2$) demonstrates IS variability predominantly below 200 km, with a noticeable periodicity of 10-30 days.

Next, the latitude-temporal structure and IS variability of DE2, DE3, DW1, and SW2 tidal components in the TIEGCM-ICON model 'Run 1' at an altitude near 100 km are examined. Figures $6a_1$-$6d_1$ present the unfiltered tidal amplitudes, while Figures $6a_2$-$6d_2$ show the same components after applying a 5-90-day filter to emphasize IS variability. The unfiltered DE2 (Figure $6a_1$) shows significant amplitude maxima primarily concentrated near the equator and around 20°S and 20°N, with periodic enhancements over time. The filtered DE2 (Figure $6a_2$) reveals that IS variability occurs across all latitudes, with pronounced peaks of around 4 m/s at equatorial and low-latitudes ($<30°$) recurring every $\sim$30-60 days. The DE3 component (Figure $6b_1$) exhibits strong amplitudes centered around the equator and extending to about 30° in both hemispheres. The filtered DE3 (Figure $6b_2$) highlights the IS variations of around 4 m/s, showing more localized and periodic enhancements, especially near the equator and low-latitudes ($<30°$), on a 30-60 day timescale. The unfiltered DW1 (Figure $6c_1$) has substantial amplitudes extending across a wide latitudinal range, with maxima of around 5 m/s near the equator and mid-latitudes ($\pm 30°$). Filtering (Figure $6c_2$) reveals IS variability in DW1 with shorter periodicities (compared to DE2 and DE3) of around 10-30 days, visible across a broad latitudinal range but most pronounced near mid-latitudes. The SW2 component (Figure 6d_1) displays distinct seasonal peaks at mid/higher latitudes (±40-60°). The filtered SW2 (Figure 6d_2) shows near to no IS variability near the equator and low latitudes (<30°), with larger amplitudes up to ∼16 m/s occurring above 45° latitude and periodic peaks occurring every 10-30 days.

Figures 7 and 8 present the same results as Figure 6, but at higher altitudes, specifically near 150 km and 300 km, respectively. The latitude structure of DE2 and DE3 undergoes significant broadening due to the effect of molecular dissipation. For example, while DE3 zonal wind amplitudes of approximately 20 m/s are confined to ±20° latitude at around 100 km altitude (Figure 6b_1), these 20 m/s DE3 zonal winds extend to latitudes as high as 40° at around 300 km (Figure 8b_1). The IS variations in both DE2 and DE3 demonstrate comparable magnitudes of approximately 4.5 m/s across all altitudes, suggesting that the source of these variations likely originates below 100 km, as no significant in situ generation of IS variability is observed. Similar observations can be made regarding the temporal variability in the filtered amplitudes for DE2 and DE3. Meanwhile, DW1 and SW2 show significantly increased amplitudes above approximately 130-150 km, as also illustrated in Figures 5c_1-5d_1, due to the in situ generation of these migrating tidal components. Interestingly, SW2 zonal winds (Figures 5d_1, 7d_1, 8d_1) display substantial lower thermospheric amplitudes (∼25 m/s) during August-September 2020, which are retained in the middle thermosphere. Their filtered amplitudes (Figures 5d_2, 7d_2, 8d_2) also exhibit prominent amplitude and vertically-coherent IS variability at all altitudes during this period. This finding aligns with the results of Maute et al. (2023), who observed large upward-propagating SW2 in TIEGCM-ICON during the 50-day period from 7 August 2020 to 27 September 2020. Maute et al. (2023) reported significant effects of sudden changes in SW2 on the upper thermosphere and ionosphere around/after 19 August 2020. These changes in SW2 are linked to the dominance of antisymmetric higher-mode HMEs post-August 2020 and are evident in Figure 5d_1. This drastic transition can be attributed to possible influences around the equinox, associated with the combined effects of transition characteristics in different altitude regions.

Figure 8 demonstrates significant ∼10− to ∼30-day variability in DW1 (and to a lesser extent in SW2) near 300 km, particularly at higher (>45°) latitudes. This periodic behavior in the migrating tides is attributable to geophysical forcing, particularly heating linked with the in situ generation of these two migrating tidal components in the middle thermosphere. Figure 9 illustrates the latitude-temporal structure of DE2, DE3, DW1, and SW2 near 300 km for the TIEGCM/ICON simulation with constant geophysical forcing (i.e., 'Run 2'). The solar/geomagnetic-driven ∼10− to ∼30-day variability in the migrating tides is absent, and the IS variations in DW1 are significantly diminished. Notably, SW2 retains substantial (±16 m/s) low-latitude IS variability, far exceeding those observed in DE2 and DE3 (±5 m/s). This IS variability in SW2 can be attributed to the upward propagating component (ref. Maute et al., 2023), as well as nonlinear interaction processes in the thermosphere, including (a) interactions between SW2 and other tides; (b) interactions with planetary waves or gravity waves; (c) modulation of background fields; and (d) coupling with ionospheric processes. It is beyond the scope of this paper to further investigate these connections; this effort is left for dedicated follow-up studies. In conclusion, Figures 5-9 collectively underscore the critical importance of tidal forcing in driving IS thermospheric variability. These results indicate that significant IS variability in tidal amplitudes propagates vertically and can considerably impact the thermospheric dynamics. These observations highlight the dynamic and complex nature of tidal forcing in the thermosphere.

As a next step, we aim to further investigate the connection between IS variability in the ZDM thermospheric winds and the MJO, as represented by the RMM1 index (ref. Figure 2d_1-2d_2). To this end, Pearson correlation analyses are performed between the filtered ZDM zonal winds, RMM1, and tidal amplitudes shown in Figures 5-9. All these time series are filtered using the method described in Section 3 to highlight IS variability. Figure 10 presents results from correlation analyses performed on the ZDM zonal winds, the near-equatorial (15°S-15°N mean) DE3 amplitudes, and the RMM1 index. Figure 10a_1 (Figure 10b_1) shows the time series of ZDM zonal winds and DE3 amplitudes (RMM1) at ∼150 km altitude. The blue lines represent the filtered ZDM zonal winds (Figure 10a_1) and RMM1 (Figure 10b_1), while the red lines depict the filtered DE3 amplitudes. Figures 10c_1-10d_1 show the same results as Figures 10a_1-10b_1 but at ∼300 km altitude.

The temporal variations in the filtered ZDM zonal winds and DE3 amplitudes exhibit concurrent fluctuations with RMM1, suggesting a plausible connection with the MJO. The correlation analysis in Figures 10a_2-10b_2 quantifies the relationship between the time series depicted in Figures 10a_1-10b_1. The lagged Pearson correlation coefficient obtained using 180-day moving windows. This moving window's length is selected to be equal to twice the maximum IS period of 90 days. The correlations reveal how the ZDM zonal winds and DE3 amplitudes may respond to changes in the MJO, with a notable correlation peak around/above r=0.6 with a positive lag of around 28 days (14 days) for the ISO (DE3), indicating that changes in RMM1 precede variations in ISO and DE3 amplitude by about 2 to 4 weeks, respectively. Figures $10c_1$ and $10d_1$ extend the analyses to a higher altitude of ∼300 km. These analyses demonstrate similar concurrent fluctuations between the RMM1 and DE3/ZDM ISO amplitudes, albeit with different magnitudes compared to the 150 km altitude. Figures $10c_2$ and $10d_2$, containing the lagged correlation coefficients at ∼300 km altitude, show similar patterns to those at ∼150 km, with a peak correlation at a positive lag but lower correlations for the ISO of around r=0.4. These results suggest that the influence of the MJO on DE3 and ZDM amplitudes extends through multiple atmospheric layers and well into the middle thermosphere. The analysis provided in Figure 10 suggests a significant interaction between the MJO, as represented by the RMM1 index, and the DE3/ZDM zonal winds in the thermosphere. The positive lag in the correlation coefficients indicates that the MJO's influence on these tidal components is consistent across different altitudes, implying a coherent vertical coupling mechanism within the atmospheric column. These findings highlight the complex dynamics of atmospheric tides and their modulation by large-scale oscillations like the MJO, which could have implications for understanding atmospheric wave coupling and energy transfer processes. Below, we performed more detailed analyses on the DE3 tide, accounting for the zonal phase propagation to unambiguously demonstrate a connection between this tidal component and the MJO.

Figure $11a_1$ presents the Hovmöller diagram of the MJO-filtered near-equatorial (20°S-20°N mean) zonal wind DE3 near 110 km altitude from TIEGCM-ICON. The color bar indicates wind deviations in m/s, with positive anomalies shown in red and negative anomalies in blue. The y-axis displays the time progression from January 2020 to January 2022, while the x-axis represents longitude. Figure $11a_2$ displays the SABER temperature DE3 similarly filtered for the MJO component. The temperature anomalies are represented in K, with the color bar indicating positive and negative anomalies. Note that the SABER DE3 tidal amplitudes and phases were obtained using 45-day moving windows, applying the tidal deconvolution method described by Oberheide et al. (2002). This method allows for the isolation and analysis of specific tidal components by filtering out other tidal and non-tidal variations. Both Figures $11a_1$ and $11a_2$ reveal the longitudinal propagation of the MJO signal, characterized by eastward propagation and alternating patterns of positive and negative anomalies every 30-90 days. These analyses confirm that the eastward propagation of DE3 is consistent with the MJO and demonstrates a high degree of self-consistency between the TIEGCM-ICON modeled and SABER observed DE3.

Figure $11b_1$ illustrates the normalized amplitudes of the DE3 tidal component, derived from the MJO-filtered series in Figures $11a_1$ and $11a_2$. The SABER MJO-filtered temperature DE3 amplitudes are depicted as a red line, while the TIEGCM MJO-filtered zonal wind DE3 amplitudes are shown as a black line. The x-axis covers the period from January 2020 to December 2022, and the y-axis represents normalized values ranging from -1 to 1. The synchronization between the red and black lines indicates a strong correlation between the temperature and wind DE3 responses to the MJO near 110 km altitude, demonstrating the coherent behavior of the MJO signal in the DE3 component in both temperature and wind fields. Some discrepancies in the temporal variability and magnitude (e.g., MJO variations of around 2.4 m/s in DE3 zonal winds versus 1.2 K in DE3 temperatures) between TIEGCM and SABER may be attributed to differences in the tidal extraction methods used and known differences in wave characteristics between temperature and wind fields (see, e.g., a related discussion in Forbes et al., 2024). Nevertheless, Figure 11 provides a comprehensive view of the MJO's influence on the DE3 tidal component, showcasing the longitudinal propagation of temperature and wind anomalies. The normalized amplitudes in Figure $11b_1$ highlight the consistent response of these anomalies to the MJO, demonstrating a strong connection between DE3 and the MJO and consistency between the MJO signal in SABER and TIEGCM DE3.

5 Conclusions

In this study, an ICON-adapted version of the TIEGCM, incorporating lower boundary tides derived from MIGHTI observations, was utilized to characterize and quantify the impact of the upward-propagating tidal spectrum on thermospheric intra-seasonal (IS) oscillations (ISOs) and to elucidate connections to the Madden-Julian Oscillation (MJO). Results show that thermospheric zonal and diurnal mean (ZDM) zonal winds exhibit prominent ($\sim$20 m/s) tidally-driven ISOs throughout 2020-2021, with the largest variations occurring at low latitudes ($\pm 30°$) near $\sim$110-150 km altitude. Correlation analyses demonstrate a robust ($r>0.6$) connection between the thermospheric ISOs, tides, and the tropospheric MJO, while Hovmöller diagrams indicate eastward tidal propagation consistent with the MJO and concurrent SABER observations.

Key findings include:

a) Tidal Contributions to Thermospheric ISOs: Results show that the diurnal/semidiurnal tidal spectrum entering the lower thermosphere near 97 km is a leading source of IS variability in the ZDM zonal wind over the whole (∼100-400 km) thermosphere. Notably, a large ∼64-day periodicity in ZDM zonal winds aligns with similar periodicities observed in OLR and RMM1 and is demonstrated to be both tidal- and MJO-related.

b) Altitude and Latitude Dependence: Altitude-time contours of ZDM zonal winds reveal that the most substantial IS variations occur in the lower thermosphere, particularly around 110-130 km. However, these variations also extend well into the middle and upper thermosphere, indicating that tidal influences penetrate multiple atmospheric layers. The latitude-time structures further highlight the complex interplay between tidal components and background wind fields, with distinct equatorially symmetric and asymmetric patterns emerging throughout the year.

c) Influence of Tidal Forcing: Comparative analysis of different TIEGCM-ICON simulations underscores the importance of tidal forcing in driving IS variability. Runs with realistic tidal forcing at the lower boundary exhibit pronounced IS variations, while simulations with constant geophysical forcing predominantly show solar/geomagnetic-induced periodicities without significant IS variations. This result highlights the critical role of tidal inputs in shaping thermospheric dynamics around IS timescales.

d) MJO-Thermosphere Interaction: Correlation analyses between the RMM1 index and the DE3/ZDM IS variations confirm a significant interaction between the MJO and thermospheric DE3 amplitudes. The positive lag in the correlation coefficients indicates that MJO variations precede changes in DE3 amplitudes, suggesting a coherent vertical coupling mechanism within the atmospheric column. This connection is evident across multiple altitudes, demonstrating the far-reaching influence of the MJO on thermospheric dynamics.

e) Hovmöller Diagram Analyses: Hovmöller diagnostics of MJO-filtered DE3 components from TIEGCM-ICON and SABER data reveal eastward propagation patterns consistent with the MJO, further corroborating the link between MJO activity and thermospheric tidal responses. The synchronization of DE3 amplitudes between TIEGCM-ICON winds and SABER temperatures underscores the coherent behavior of the MJO influence in the thermosphere.

This study underscores the intricate dynamics of atmospheric tides and their modulation by large-scale tropospheric oscillations, such as the MJO. These interactions have profound implications for the global understanding of wave coupling and energy transfer processes. Our findings reveal the complex interplay between lower atmospheric processes and thermospheric dynamics on IS time scales, highlighting the necessity for comprehensive modeling and observational frameworks to enhance our understanding of vertical coupling mechanisms. Improving our understanding of the thermosphere has widespread practical applications that benefit satellite operations, communication systems, weather and climate prediction, defense and security, scientific research, and aviation.

Future research should focus on further quantifying these interactions and exploring their implications for thermosphere-ionosphere (T-I) states and dynamics. These efforts are expected to provide valuable insights for the development of predictive capabilities that connect tropical tropospheric weather to space weather of the T-I system. This study also emphasizes the critical need for detailed investigations into the vertical and horizontal coupling mechanisms within the 'thermospheric gap' region, spanning approximately 100 to 300 km. Such investigations will be uniquely enabled by a new dedicated satellite mission designed to provide simultaneous global measurements of this region.

6 Open Research Section

TIEGCM-ICON output is publicly available via NASA's Space Physics Data Facility (SPDF) at `https://spdf.gsfc.nasa.gov/pub/data/icon/l2/` and via ICON's public site `https://icon.ssl.berkeley.edu/Data`. The Kp index is obtained from GFZ Potsdam at `https://kp.gfz-potsdam.de/app/files/Kp_ap_since_1932.txt`, the F10.7 cm radio flux from NASA/GSFC OMNIWeb at `https://omniweb.gsfc.nasa.gov/form/dx1.html`. NOAA Interpolated Outgoing Longwave Radiation (OLR) data and RMM index values are publicly provided by the NOAA Physical Sciences Laboratory (PSL) from their website at `https://psl.noaa.gov`. The post-processed data used to produce Figures 1-11 are publicly available via Zenodo at the following doi: 10.5281/zenodo.12744700.

Acknowledgments

FG acknowledges support from NSF grants 2113411 and 2223930; NASA grants 80NSSC22K0019 and 80NSSC22K1010; and AFOSR grant FA9550-22-1-0328. ICON is supported by NASA's Explorers Program through contracts NNG12FA45C and NNG12FA42I. AM acknowledges support from NASA ICON award 80NSSC23K1123 and NASA LWS award 80NSSC20K1784.

References

Alken, P., Thébault, E., Beggan, C.D. et al. (2021). International Geomagnetic Reference Field: the thirteenth generation. Earth Planets Space 73, 49. https://doi.org/10.1186/s40623-020-01288-x.

Andrews, D. G., Holton, J. R., & Leovy, C. B. (1987). Middle Atmospheric Dynamics. Academic Press, 489.

Chang, L. C., Palo, S. E., & Liu, H. (2011). Short-term variability in the migrating diurnal tide caused by interactions with the quasi 2 day wave. Journal of Geophysical Research, 116, D12112. https://doi.org/10.1029/2010JD014996.

Chapman S.; Lindzen R.S.. (1970) Atmospheric Tides. Reidel: Dordrecht.

Cullens, C. Y., Immel, T. J., Triplett, C. C., Wu, Y. J., England, S. L., Forbes, J. M., & Liu, G. (2020). Sensitivity study for ICON tidal analysis. Progress in Earth and Planetary Science, 7(1), 18. https://doi.org/10.1186/s40645-020-00330-6.

Cullens, C. Y., England, S. L., Immel, T. J., Maute, A., Harding, B. J., Triplett, C. C., et al. (2022). Seasonal variations of medium-scale waves observed by icon-mighti. Geophys. Res. Lett. 49, e2022GL099383. doi:10.1029/2022gl099383

Dickinson, R. E., Infrared radiative cooling in the mesosphere and lower thermosphere, J. Atmos. Terr. Phys., 46, 995-1008, 1984.

Drob, D.P. et al., An update to the horizontal wind model (HWM): the quiet time thermosphere. Earth Space Sci. 2(7), 301–319 (2015). doi:10.1002/2014EA000089

Eckermann, S. D., Rajopadhyaya, D. K., & Vincent, R. A. (1997). Intraseasonal wind variability in the equatorial mesosphere and lower thermosphere: Long-term observations from the central Pacific. Journal of Atmospheric and Solar-Terrestrial Physics, 59(6), 603–627. https://doi.org/10.1016/S1364-6826(96)00143-5.

Forbes, J. M., Zhang, X., Palo, S. E., et al. (2009). Kelvin waves in stratosphere, mesosphere and lower thermosphere temperatures as observed by TIMED/SABER during 2002-2006. Earth Planets and Space, 61, 447-453.

Forbes, J. M., Bruinsma, S., & Lemoine, F. G. (2006). Solar rotation effects on the thermospheres of Mars and Earth. Science, 312(5778), 1366–1368. https://doi.org/10.1126/science.1126389.

Forbes, J. M., & Zhang, X. (2022). Hough Mode Extensions (HMEs) and solar tide behavior in the dissipative thermosphere. Journal of Geophysical Research: Space Physics, 127, e2022JA030962. https://doi.org/10.1029/2022JA030962.

Forbes, J. M., Zhang, X., Englert, C. R., Heelis, R., Stevens, M. H., Harding, B. J., et al. (2024). Thermosphere UFKW structures and ionosphere coupling as observed by ICON. Geophysical Research Letters, 51, e2023GL105975. https://doi.org/10.1029/2023GL105975

Forbes, J. M., Zhang, X., & Palo, S. E. (2023). UFKW propagation in the dissipative thermosphere. Journal of Geophysical Research: Space Physics, 128(1), e2022JA030921. https://doi.org/10.1029/2022JA030921.

Forbes, J. M. (2000). Wave coupling between the lower and upper atmosphere: Case study of an ultra-fast Kelvin wave. Journal of Atmospheric and Solar-Terrestrial Physics, 62, 1603–1621.

Forbes, J. M., & Vincent, R. A. (1989). Effects of mean winds and dissipation on the diurnal propagating tide: An analytic approach. Planetary and Space Science, 37, 197-209.

Forbes, J. M., Zhang, X., Hagan, M. E., England, S. L., Liu, G., & Gasperini, F. (2017). On the specification of upward-propagating tides for ICON science investigations. Space Science Reviews, 212(1–2), 697–713. https://doi.org/10.1007/s11214-017-0401-5.

Forbes, J. M., Bruinsma, S., & Lemoine, F. G. (2006). Solar rotation effects on the thermospheres of Mars and Earth. Science, 312(5778), 1366–1368. https://doi.org/10.1126/science.1126389.

Forbes, J. M., Heelis, R., Zhang, X., Englert, C. R., Harding, B. J., He, M., Chau, J. L., Stoneback, R., Harlander, J. M., Marr, K. D., & Makela, J. J. (2021a). Q2DW-tide and-ionosphere interactions as observed from ICON and ground-based radars. J. Geophys. Res. Space Phys.

https://doi.org/10.1029/2021JA029961

Forbes, J. M., Hagan, M. E., Thermospheric extensions of the classical expansion functions for semidiurnal tides. J. Geophys. Res. Space Phys. 87(A7), 5253–5259 (1982). doi:10.1029/JA087iA07p05253

Forbes, J. M., Oberheide, J., Zhang, X., Cullens, C., Englert, C. R., Harding, B. J., et al. (2022). Vertical coupling by solar semidiurnal tides in the thermosphere from ICON/MIGHTI measurements. Journal of Geophysical Research: Space Physics, 127, e2022JA030288. https://doi.org/10.1029/2022JA030288

Forbes, J. M., Oberheide, J., Zhang, X., Cullens, C., Englert, C. R., Harding, B. J., et al. (2024). Thermosphere UFKW structures and ionosphere coupling as observed by ICON. Geophysical Research Letters, 51, e2023GL105975. https://doi.org/10.1029/2023GL105975

Forbes, J. M., Zhang, X., Heelis, R., Stoneback, R., Englert, C. R., Harlander, J. M., et al. (2021b). Atmosphere-ionosphere (A-I) coupling as viewed by ICON: day-to-day variability due to planetary wave (PW)-tide interactions. J. Geophys. Res. Space Phys. 126:e2020JA028927. https://doi.org/10.1029/2020JA028927

Forbes, J. M., Zhang, X., Palo, S. E., et al. (2009). Kelvin waves in stratosphere, mesosphere and lower thermosphere temperatures as observed by TIMED/SABER during 2002-2006. Earth Planets and Space, 61, 447-453.

Forbes, J. M., Zhang, X. (2022). Hough mode extensions (HMEs) and solar tide behavior in the dissipative thermosphere. J. Geophys. Res. Space Phys. 127, e2022JA030962. doi:10.1029/2022JA030962

Forbes J.M.. (1995) Tidal and planetary waves. Geophysics Monographs 87 67–87.

Fritts, D. C., & Alexander, M. J. (2003). Gravity wave dynamics and effects in the middle atmosphere. Reviews of Geophysics, 41, 1003.

Gasperini, F., Forbes, J. M., Doornbos, E. N., & Bruinsma, S. L. (2015). Wave coupling between the lower and middle thermosphere as viewed from TIMED and GOCE. Journal of Geophysical Research, 120, 5788-5804. https://doi.org/10.1002/2015JA021300.

Gasperini, F., Hagan, M. E., & Zhao, Y. (2017a). Evidence of tropospheric 90-day oscillations in the thermosphere. Geophysical Research Letters. https://doi.org/10.1002/2017GL075445.

Gasperini, F., Forbes, J. M., & Hagan, M. E. (2017b). Wave coupling from the lower to the middle thermosphere: Effects of mean winds and dissipation. Journal of Geophysical Research, 122, 7781-7797. https://doi.org/10.1002/2017JA024317.

Gasperini, F., Forbes, J. M., Doornbos, E. N., & Bruinsma, S. L. (2018). Kelvin wave coupling from TIMED and GOCE: Inter/intra-annual variability and solar activity effects. Journal of Atmospheric and Solar-Terrestrial Physics, 171, 176-187. https://doi.org/10.1016/j.jastp.2017.08.034.

Gasperini, F., Liu, H., & McInerney, J. (2020). Preliminary evidence of Madden-Julian Oscillation effects on ultrafast tropical waves in the thermosphere. Journal of Geophysical Research, 125, e2019JA027649. https://doi.org/10.1029/2019JA027649.

Gasperini, F., Azeem, I., Crowley, G., Perdue, M., Depew, M., Immel, T., et al. (2021). Dynamical coupling between the low-latitude lower thermosphere and ionosphere via the nonmigrating diurnal tide as revealed by concurrent satellite observations and numerical modeling. Geophysical Research Letters, 48, e2021GL093277. https://doi.org/10.1029/2021GL093277.

Gasperini, F., Crowley, G., Immel, T. J. et al. (2022). Vertical Wave Coupling in the Low-Latitude Ionosphere-Thermosphere as Revealed by Concurrent ICON and COSMIC-2 Observations. Space Science Reviews, 218, 55. https://doi.org/10.1007/s11214-022-00923-1.

Gasperini, F., Jones, M., Jr, Harding, B. J., & Immel, T. J. (2023a). Direct observational evidence of altered mesosphere lower thermosphere mean circulation from a major sudden stratospheric warming. Geophysical Research Letters, 50, e2022GL102579. https://doi.org/10.1029/2022GL102579.

Gasperini, F., Harding, B. J., Crowley, G., & Immel, T. J. (2023b). Ionosphere-thermosphere coupling via global-scale waves: new insights from two years of concurrent in situ and remotely-sensed satellite observations. Frontiers in Astronomy and Space Sciences, 10, 1217737. https://doi.org/10.3389/fspas.2023.1217737.

Gasperini, F., Jr., M. J., Moffat-Griffin, T., Marsh, D., Cullens, C., & Knizova, P. K. (2023c). Ionosphere-Thermosphere-Mesosphere Variability imposed by Waves from Below in Future Climates. Bulletin of the AAS, 55(3). https://doi.org/10.3847/25c2cfeb.c3db219f.

Gasperini, F., & Oberheide, J. (2024). Dynamical Meteorology: Atmospheric Tides. https://doi.org/10.1016/B978-0-323-96026-7.00073-4.

Gruber, A., & Winston, J. S. (1978). Earth-Atmosphere Radiative Heating Based on NOAA Scanning Radiometer Measurements. Bulletin of the American Meteorological Society, 59, 1570-1573.

Gu, S.-Y., Dou, X., Lei, J., Li, T., Luan, X., Wan, W., & Russell III, J. M. (2014). Ionospheric response to the ultrafast Kelvin wave in the MLT region. Journal of Geophysical Research, 119, 1369-1380. https://doi.org/10.1002/2013JA019086.

Hagan, M., Forbes, J., & Vial, F. (1995). On modeling migrating solar tides. Geophysical Research Letters, 22(8), 893-896. https://doi.org/10.1029/95GL00783

Harding, B. J. (2023). Ionospheric Connection Explorer (ICON) conjugate maneuver data used in Harding et al. (2023, submitted) [Dataset]. Zenodo. https://doi.org/10.5281/zenodo.8436866.

Harding, B. J., Chau, J. L., He, M., Englert, C. R., Harlander, J. M., Marr, K. D., et al. (2021). Validation of ICON-MIGHTI thermospheric wind observations: 2. Green-line comparisons to specular meteor radars. Journal of Geophysical Research: Space Physics, 126(3), 1–12. https://doi.org/10.1029/2020JA028947.

Hayashi, Y. (1971). A generalized method of resolving disturbances into progressive and retrogressive waves by space Fourier and time cross-spectral analyses. Journal of the Meteorological Society of Japan. Series II, 49, 125-128. $https://doi.org/10.2151/jmsj1965.49.2_1 25$.

Immel, T.J., England, S.L., Mende, S.B., et. al. (2018). The Ionospheric Connection Explorer mission: mission goals and design. Space Sci Rev 214:13. https://doi.org/10.1007/s11214-017-0449-2

Immel, T.J., Harding, B.J., Heelis, R.A., Maute, A., Forbes, J.M., England, S.L., et al. (2021). Regulation of ionospheric plasma velocities by thermospheric winds. Nat Geosci 14:893–898. https://doi.org/10.1038/s41561-021-00848-4

Immel, T.J., Eastes, R.W. (2019). New NASA missions focus on terrestrial forcing of the space environment. Bull Am Meteorol Soc 100:2153–2156. https://doi.org/10.1175/BAMS-D-19-0066.1

Jones, M., Forbes, J. M., Hagan, M. E., and Maute, A. (2014). Impacts of vertically propagating tides on the mean state of the ionosphere-thermosphere system. J.

Geophys. Res. Space Phys. 119, 2197–2213.

Johnson, E. S., & Heelis, R. A. (2005). Characteristics of ion velocity structure at high latitudes during steady southward interplanetary magnetic field conditions. Journal of Geophysical Research, 110, 148-227.

Kayano, M. T., V. E. Kousky, and J. E. Janowiak, 1995: Outgoing longwave radiation bias and their impacts on EOF modes of interannual variability in the Tropics. J. Geophys. Res.,100, 3173–3195.

Karoly, D. J., Roff, G. L., & Reeder, M. J. (1996). Gravity wave activity associated with tropical convection detected in TOGA COARE sounding data. Geophysical Research Letters, 23(3), 261–264. https://doi.org/10.1029/96GL00023.

Kumari, K., Oberheide, J., & Lu, X. (2020). The tidal response in the mesosphere/lower thermosphere to the Madden-Julian oscillation observed by SABER. Geophysical Research Letters, 47, e2020GL089172. https://doi.org/10.1029/2020GL089172.

Kumari, K., Wu, H., Long, A., Lu, X., & Oberheide, J. (2021). Mechanism studies of Madden-Julian Oscillation coupling into the mesosphere/lower thermosphere tides using SABER, MERRA-2, and SD-WACCMX. Journal of Geophysical Research: Atmospheres, 126, e2021JD034595. https://doi.org/10.1029/2021JD034595.

Lieberman, R. S. (1998). Intraseasonal variability of high-resolution Doppler imager winds in the equatorial mesosphere and lower thermosphere. Journal of Geophysical Research, 103, 11221-11228.

Lieberman, R. S., Riggin, D. M., Ortland, D. A., Nesbitt, S. W., & Vincent, R. A. (2007). Variability of mesospheric diurnal tides and tropospheric diurnal heating during 1997-1998. Journal of Geophysical Research, 112, D20110. https://doi.org/10.1029/2007JD008578.

Liebmann, B., & Smith, C. A. (1996). Description of a complete (interpolated) Outgoing Longwave Radiation dataset. Bulletin of the American Meteorological Society, 77, 1275-1277.

Lindzen, R. S., & Hong, S. S. (1974). Effects of mean winds and horizontal temperature gradients on solar and lunar semidiurnal tides in the atmosphere. Journal of the Atmospheric Sciences, 31, 1421–1446.

Liu, H. -L. (2016). Variability and predictability of the space environment as related to lower atmosphere forcing. Space Weather, 14, 634-658. https://doi.org/10.1002/2016SW001450.

Liu, Y., San Liang, X., & Weisberg, R. H. (2007). Rectification of the bias in the wavelet power spectrum. Journal of Atmospheric and Oceanic Technology, 24(12), 2093–2102. https://doi.org/10.1175/2007JTECHO511.1.

Madden, R. A., & Julian, P. R. (1971). Detection of a 40-50 day oscillation in the zonal wind in the tropical Pacific. Journal of Geophysical Research, 28, 702-708.

Madden, R. A., & Julian, P. R. (1994). Observations of the 40-50-day tropical oscillation: A review. Monthly Weather Review, 122, 814-837. https://doi.org/10.1175/1520-0493(1994)122¡0814:OOTDTO¿2.0.CO;2.

Matsushita, S.. (1967a) Solar quiet and lunar daily variation fields. In: (editors: Matsushita S.; Campbell W.H..) Physics of Geomagnetic Phenomena. Academic Press: New York, pp. 301–427.

Matsushita, S.. (1967b) Lunar tides in the ionosphere. In: Handbuch der Physik. Springer-Verlag: Berlin, pp. 547–602.

Maute, A. (2017). Thermosphere-ionosphere-electrodynamics general circulation model for the ionospheric connection explorer: TIEGCM-ICON. Space Science Reviews, 212, 523-551. https://doi.org/10.1007/s11214-017-0330-3.

Maute, A., Forbes, J. M., Cullens, C. Y., & Immel, T. J. (2023). Delineating the effect of upward propagating migrating solar tides with the TIEGCM-ICON. Frontiers in Astronomy and Space Sciences, 10, 1147571. https://doi.org/10.3389/fspas.2023.1147571.

Moss, A. C., Wright, C. J., & Mitchell, N. J. (2016). Does the Madden-Julian oscillation modulate stratospheric gravity waves? Geophysical Research Letters, 43, 3973–3981. https://doi.org/10.1002/2016GL068498.

Oberheide, J., Hagan, M. E., Roble, R. G., & Offermann, D. (2002). Sources of nonmigrating tides in the tropical middle atmosphere. Journal of Geophysical Research, 107(D21), 4567. https://doi.org/10.1029/2002JD002220.

Oberheide, J., Forbes, J. M., Zhang, X., and Bruinsma, S. L. (2011a). Climatology of upward propagating diurnal and semidiurnal tides in the thermosphere. J. Geophys. Res. 116. doi:10.1029/2011JA01678

Oberheide, J., Forbes, J. M., Zhang, X., and Bruinsma, S. L. (2011b). Wave-driven variability in the ionosphere-thermosphere-mesosphere system from TIMED observations: What contributes to the "wave 4. J. Geophys. Res. 116. doi:10.1029/2010JA015911

Palo, S. E., R. G. Roble, and M. E. Hagan (1999). Middle atmosphere effects of the quasi-two-day wave determined from a General Circulation Model. Earth Planets Space, 51, 629–647.

Pancheva, D., Miyoshi, Y., Mukhtarov, P., Jin, H., Shinagawa, H. H., & Fujiwara, H. (2012). Global response of the ionosphere to atmospheric tides forced from below: Comparison between cosmic measurements and simulations by atmosphere-ionosphere coupled model GAIA. Journal of Geophysical Research, 117.

Picone, J.M., Hedin, A.E., Drob, D.P., Aikin, A.C. (2002). Nrlmsise-00 empirical model of the atmosphere: Statistical comparisons and scientific issues. J. Geophys. Res. Space Phys. doi:10.1029/2002JA009430

Qian, L., Burns, A. G., Emery, B. A., Foster, B., Lu, G., Maute, A., Richmond, A. D., Roble, R. G., Solomon, S. C., & Wang, W. (2014). The NCAR TIE-GCM. In Modeling the Ionosphere–Thermosphere System (eds J. Huba, R. Schunk, & G. Khazanov). https://doi.org/10.1002/9781118704417.ch7.

Qian, L., & Solomon, S. C. (2012). Thermospheric Density: An Overview of Temporal and Spatial Variations. Space Science Reviews, 168, 147–173. https://doi.org/10.1007/s11214-011-9810-z.

Richards, P., J. Fennelly, D. Torr (1994). EUVAC: a solar EUV flux model for aeronomic calculations. J. Geophys. Res. 99, 8981–8992

Richmond, A.D., E.C. Ridley, R.G. Roble (1992). A thermosphere/ionosphere general circulation model with coupled electrodynamics. Geophys. Res. Lett. 19(6), 601–604. doi:10.1029/92GL00401

Richmond, A.D., Maute, A. (2013). Ionospheric electrodynamics modeling, in Modeling the Ionosphere-Thermosphere, ed. by R.S.J.D. Huba, G. Khazanov. AGU Geophysical Monograph Series, vol. 201 (Wiley, Chichester, p. 417). doi:10.1002/9781118704

Richmond, A. (1995). Ionospheric electrodynamics using magnetic apex coordinates. J. Geomagnetism Geoelectr. 47, 191–212. doi:10.5636/jgg.47.191

Roble, R., Ridley, E. (1987). An auroral model for the NCAR thermospheric general circulation model (TGCM). United States: Annales Geophysicae 5A, 369–382.

Roble, R., Ridley, E., Richmond, A. (1988). A coupled thermosphere/ionosphere general circulation model. Geophys. Res. Lett. 15, 1325–1328.

Salby ML, Hartmann DL, Bailey PL, Gille JC (1984) Evidence for equatorial Kelvin modes in Nimbus-7 LIMS. J Atmos Sci 41:220–235

Sassi, F., McCormack, J. P., & McDonald, S. E. (2019). Whole atmosphere coupling on intraseasonal and interseasonal time scales: A potential source of increased predictive capability. Radio Science, 54, 913-933. https://doi.org/10.1029/2019RS006847.

Sutton, J.P. Thayer, W. Wang, S.C. Solomon, X. Liu, B.T. Foster, A self-consistent model of helium in the thermosphere. J. Geophys. Res. Space Phys. 120(8), 6884–6900 (2015). doi:10.1002/2015JA021223

Stevens, M. H., Englert, C. R., Harlander, J. M. et al. (2022). Temperatures in the Upper Mesosphere and Lower Thermosphere from O2 Atmospheric Band Emission Observed by ICON/MIGHTI. Space Science Reviews, 218, 67. https://doi.org/10.1007/s11214-022-00935-x.

Thayer, J. P., & Semeter, J. (2004). The convergence of magnetospheric energy flux in the polar atmosphere. Journal of Atmospheric and Solar-Terrestrial Physics, 66, 807-824.

Tian, B., Ao, C. O., Waliser, D. E., Fetzer, E. J., Mannucci, A. J., & Teixeira, J. (2012). Intraseasonal temperature variability in the upper troposphere and lower stratosphere from GPS radio occultation measurements. Journal of Geophysical Research, 117, D15110. https://doi.org/10.1029/2012JD017715.

Torrence, C., & Compo, G. P. (1998). A practical guide to wavelet analysis. Bulletin of the American Meteorological Society, 79, 61–78. https://doi.org/10.1175/1520-0477(1998)079¡0061:APGTWA¿2.0.CO;2.

Truskowski, A., Forbes, J. M., Zhang, X., & Palo, S. (2014). New perspectives on thermosphere tides: 1. Lower thermosphere spectra and seasonal-latitudinal structures. Earth, Planets and Space, 66, 136. https://doi.org/10.1186/s40623-014-0136-4.

Vergados, P., Liu, G., Mannucci, A. J., & Janches, D. (2018). Equatorial intraseasonal temperature oscillations in the lower thermosphere from SABER. Geophysical Research Letters, 45, 10893-10902. https://doi.org/10.1029/2018GL079467.

Walterscheid, R. L., & Venkateswaran, S. V. (1979a). Influence of mean zonal motion and meridional temperature gradients on the solar semidiurnal atmospheric tide: A spectral study. Part I: Theory. Journal of the Atmospheric Sciences, 36, 1623–1635.

Walterscheid, R. L., & Venkateswaran, S. V. (1979b). Influence of mean zonal motion and meridional temperature gradients on the solar semidiurnal atmospheric tide: A spectral study. Part II: Numerical results. Journal of the Atmospheric Sciences, 36, 1636–1662.

Weimer, D. R. (2005). Improved ionospheric electrodynamic models and application to calculating Joule heating rates. J. Geophys. Res. 110, A05306. doi:10.1029/2004JA010884

Wheeler, M., & Hendon, H. H. (2004). An all-season real-time multivariate MJO index: Development of an index for monitoring and prediction. Monthly Weather Review, 132(8), 1917-1932. https://doi.org/10.1175/1520-0493(2004)132¡1917:AARMMI¿2.0.CO;2.

Wheeler, M., & Kiladis, G. N. (1999). Convectively coupled equatorial waves: Analysis of clouds and temperature in the wavenumber-frequency domain. Journal of the Atmospheric Sciences, 56(3), 374-399. https://doi.org/10.1175/1520-0469(1999)056¡0374:CCEWAO¿2.0.CO;2.

Wu, D. L., Hays, P. B., & Skinner, W. R. (1995). A least squares method for spectral analysis of space-time series. Journal of the Atmospheric Sciences, 52, 3501–3511. https://doi.org/10.1175/1520-0469(1995)052¡3501:ALSMFS¿2.0.CO;2.

Yamazaki, Y. (2023). A method to derive Fourier-wavelet spectra for the characterization of global-scale waves in the mesosphere and lower thermosphere and its MATLAB and Python software.

Yang, C., Smith, A. K., Li, T., & Dou, X. (2018). The effect of the Madden-Julian Oscillation on the mesospheric migrating diurnal tide: A study using SD-WACCM. Geophysical Research Letters, 45, 5105-5114. https://doi.org/10.1029/2018GL077956.

Yiğit, E., & Medvedev, A. S. (2015). Internal wave coupling processes in Earth's atmosphere. Advances in Space Research, 55, 983-1003.

Zhang, C. (2005). Madden-Julian oscillation. Reviews of Geophysics, 43, RG2003. https://doi.org/10.1029/2004RG000158.

Figure 1. Time series of daily Kp and F10.7 values (panels a_1 and b_1) before (black lines) and after (blue lines) a 5-90-day filter is applied. The respective Morlet wavelets are shown in panels a_2 and b_2. Similarly, time series (wavelets) of equatorial ($\pm 15^\circ$ latitude mean) OLR and RMM1 amplitudes are shown in panels c_1 and d_1 (c_2 and d_2), respectively.

Figure 2. Time series of zonal and diurnal mean (ZDM) zonal winds near the equator (±15° latitude mean) and 150 km altitude for TIEGCM-ICON ‘Run 1’

Figure 3. (a_1) Altitude (∼100-400 km) versus time (month-of-year, moy, since January 2020) contours of TIEGCM-ICON ZDM zonal wind (m/s) near the

Figure 4. Altitude (∼100-400 km) versus latitude (60°S-60°N) contours of ZDM zonal winds centered on 10 October 2020 for TIEGCM 'Run 1' (a_1), 'Run 1' - 'Run 3' (a_2), and filtered 'Run 1' - 'Run 3' (a_3). (b_1)-(b_3) Same as (a_1)-(a_3), but centered on 10 November 2020.

Figure 5. TIEGCM-ICON 'Run 1' zonal wind DE2 (panel a_1), DE3 (panel b_1), DW1 (panel c_1), and SW2 (panel d_1) amplitudes near the equator (15°S-15°N mean) as a function of altitude (∼100-400 km) and time (months since January 2020). Panels a_2-d_2 show the tidal amplitudes of DE2, DE3, DW1, and SW2, respectively, after a 5-90-day filter is applied.

Figure 6. Latitude (60°S-60°N) versus time (months since January 2020) contours of TIEGCM-ICON 'Run 1' zonal wind DE2 (panel a_1), DE3 (panel a_2), DW1 (panel a_3), and SW2 (panel a_4) amplitudes near 100 km altitude. (a_2)-(d_2) Same as a_1)-(d_1), but with a 5-90-day filter applied.

Figure 7. Same as Figure 6, but near 150 km altitude.

Figure 8. Same as Figure 6, but near 300 km altitude.

Figure 9. Same as Figure 8, but for the TIEGCM-ICON 'Run 2' with constant geophysical forcing.

Figure 10. Time series near 150 km (a_1) of 5-90-day filtered near-equatorial (15°S-15°N) ZDM ISO (blue line, left y-axis) and DE3 zonal wind (red line, right y-axis) amplitudes and their lagged Pearson correlation coefficient (a_2) obtained on 180-day moving windows from January 2020 to December 2021. (b_1)-(b_2) Same as panels a_1-a_2, but for RMM1 and near-equatorial DE3 zonal wind amplitudes. (c_1)-(c_2) and (d_1)-(d_2) Same as (a_1)-(a_2), and (b_1)-(b_2), respectively, but near 300 km altitude. The DE3 zonal winds and ZDM ISOs are derived from TIEGCM-ICON 'Run 1' output.

Figure 11. Hovmöeller MJO analyses of DE3 during 2020-2021 near 110 km altitude and the equator (20°S-20°N mean) for TIEGCM-ICON zonal wind (a_1) and SABER temperature (panel a_2). The SABER DE3 amplitude and phases are obtained from 45-day moving windows using the tidal deconvolution method by Oberheide et al. (2002). (b_1) Normalized DE3 amplitudes based on the MJO filtered series in panels (a_1)-(a_2), with SABER temperature DE3 shown as a red line and TIEGCM zonal wind DE3 shown as a black line.

Figure 1.

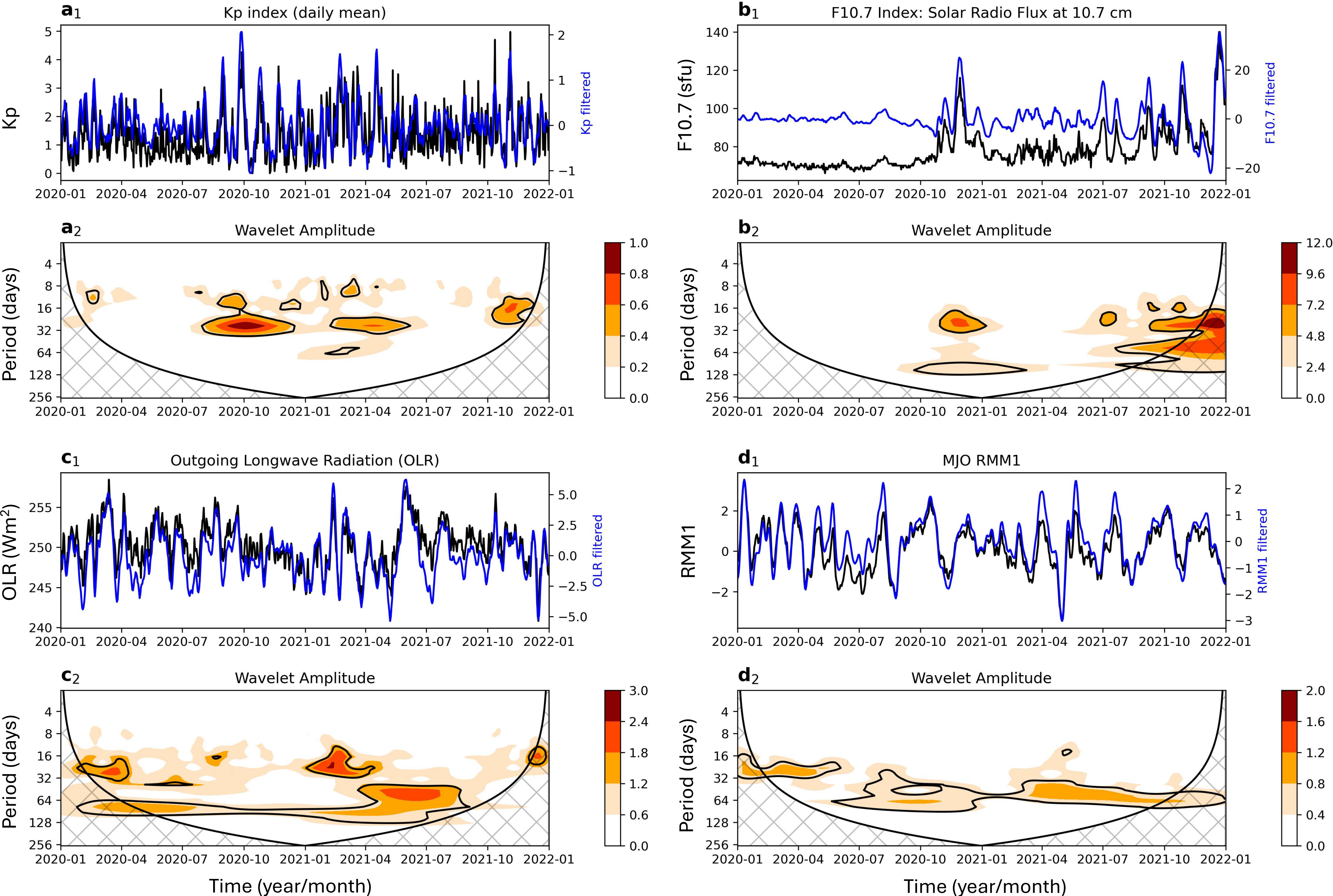

a1
Kp index (daily mean)
Kp
Kp filtered
b1
F10.7 Index: Solar Radio Flux at 10.7 cm
F10.7 (sfu)
F10.7 filtered
a2
Wavelet Amplitude
Period (days)
b2
Wavelet Amplitude
Period (days)
c1
Outgoing Longwave Radiation (OLR)
OLR (Wm2)
OLR filtered
d1
MJO RMM1
RMM1
RMM1 filtered
c2
Wavelet Amplitude
Period (days)
d2
Wavelet Amplitude
Period (days)
Time (year/month)
Time (year/month)

Figure 2.

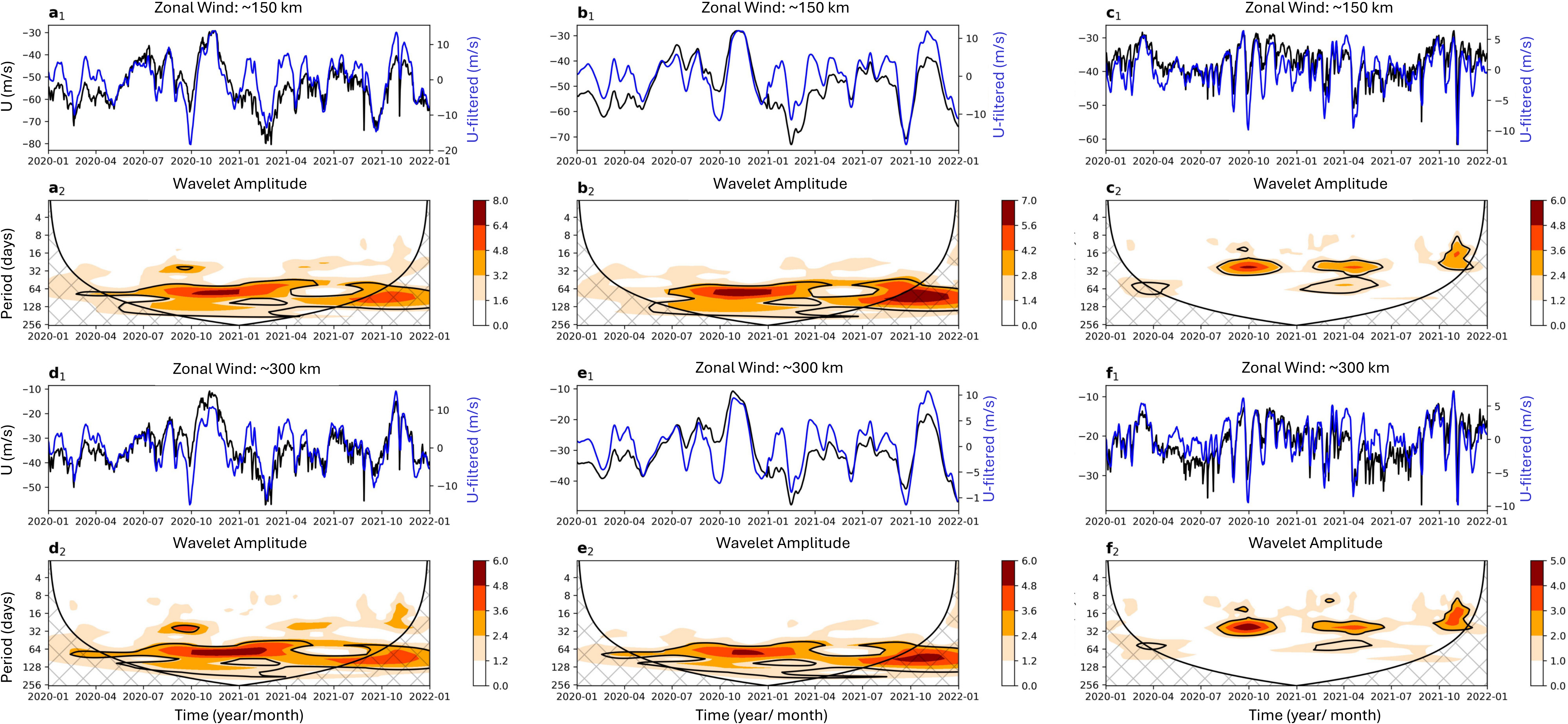

a1 Zonal Wind: ~150 km
b1 Zonal Wind: ~150 km
c1 Zonal Wind: ~150 km
U (m/s)
U-filtered (m/s)
a2 Wavelet Amplitude
b2 Wavelet Amplitude
c2 Wavelet Amplitude
Period (days)
d1 Zonal Wind: ~300 km
e1 Zonal Wind: ~300 km
f1 Zonal Wind: ~300 km
d2 Wavelet Amplitude
e2 Wavelet Amplitude
f2 Wavelet Amplitude
Time (year/month)
Time (year/ month)
Time (year/ month)

Figure 3.

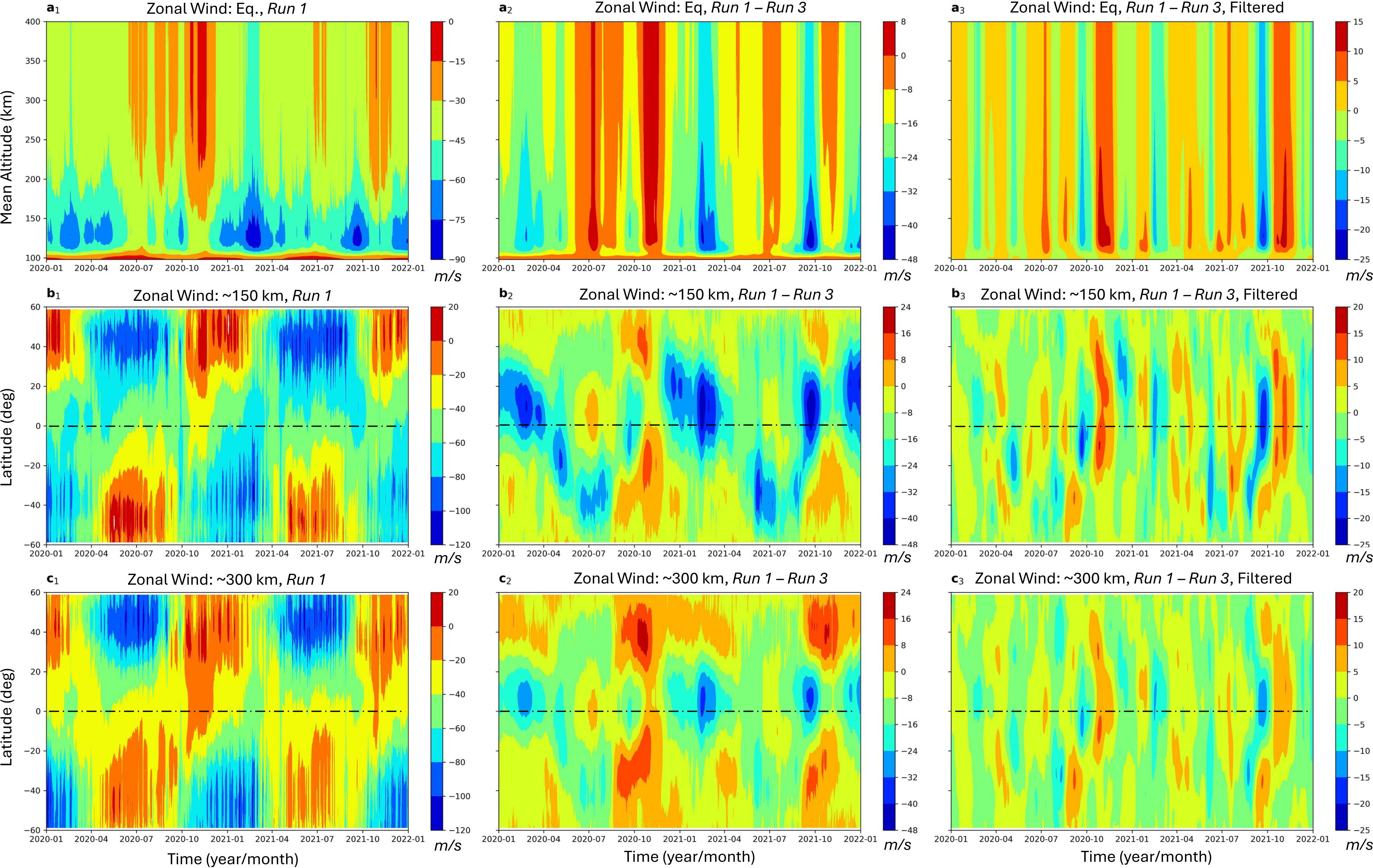
a1 Zonal Wind: Eq., Run 1
a2 Zonal Wind: Eq, Run 1 – Run 3
a3 Zonal Wind: Eq, Run 1 – Run 3, Filtered
b1 Zonal Wind: ~150 km, Run 1
b2 Zonal Wind: ~150 km, Run 1 – Run 3
b3 Zonal Wind: ~150 km, Run 1 – Run 3, Filtered
c1 Zonal Wind: ~300 km, Run 1
c2 Zonal Wind: ~300 km, Run 1 – Run 3
c3 Zonal Wind: ~300 km, Run 1 – Run 3, Filtered
Mean Altitude (km)
100
150
200
250
300
350
400
Latitude (deg)
-60
-40
-20
0
20
40
60
2020-01
2020-04
2020-07
2020-10
2021-01
2021-04
2021-07
2021-10
2022-01
Time (year/month)
m/s
0
-15
-30
-45
-60
-75
-90
8
0
-8
-16
-24
-32
-40
-48
15
10
5
0
-5
-10
-15
-20
-25
20
0
-20
-40
-60
-80
-100
-120
24
16
8
0
-8
-16
-24
-32
-40
-48
20
15
10
5
0
-5
-10
-15
-20
-25

Figure 4.

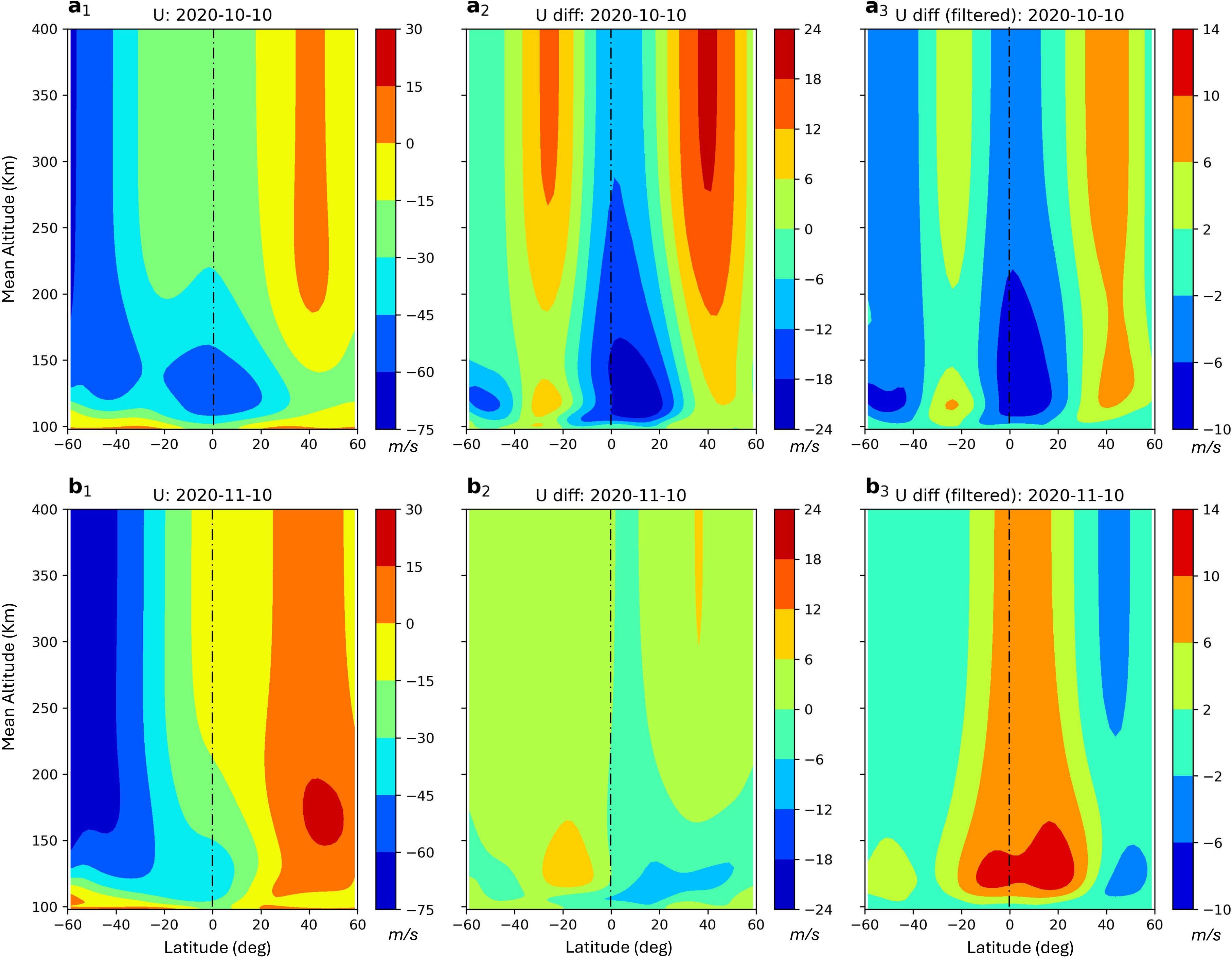

a1
U: 2020-10-10
a2
U diff: 2020-10-10
a3
U diff (filtered): 2020-10-10
b1
U: 2020-11-10
b2
U diff: 2020-11-10
b3
U diff (filtered): 2020-11-10
Mean Altitude (Km)
Latitude (deg)
m/s

Figure 5.

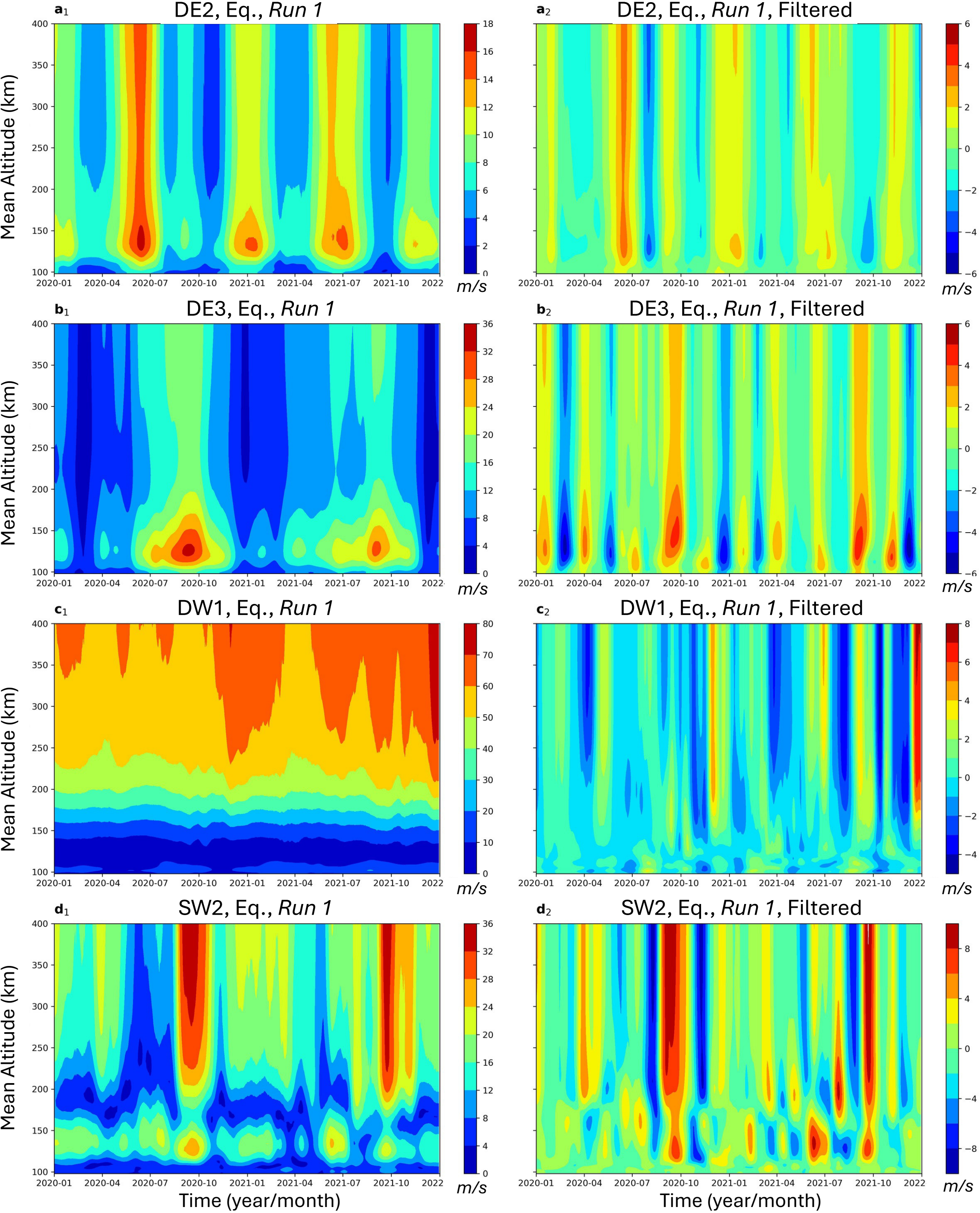
a1 DE2, Eq., Run 1
a2 DE2, Eq., Run 1, Filtered
b1 DE3, Eq., Run 1
b2 DE3, Eq., Run 1, Filtered
c1 DW1, Eq., Run 1
c2 DW1, Eq., Run 1, Filtered
d1 SW2, Eq., Run 1
d2 SW2, Eq., Run 1, Filtered
Mean Altitude (km)
Time (year/month)
m/s
2020-01
2020-04
2020-07
2020-10
2021-01
2021-04
2021-07
2021-10
2022

Figure 6.

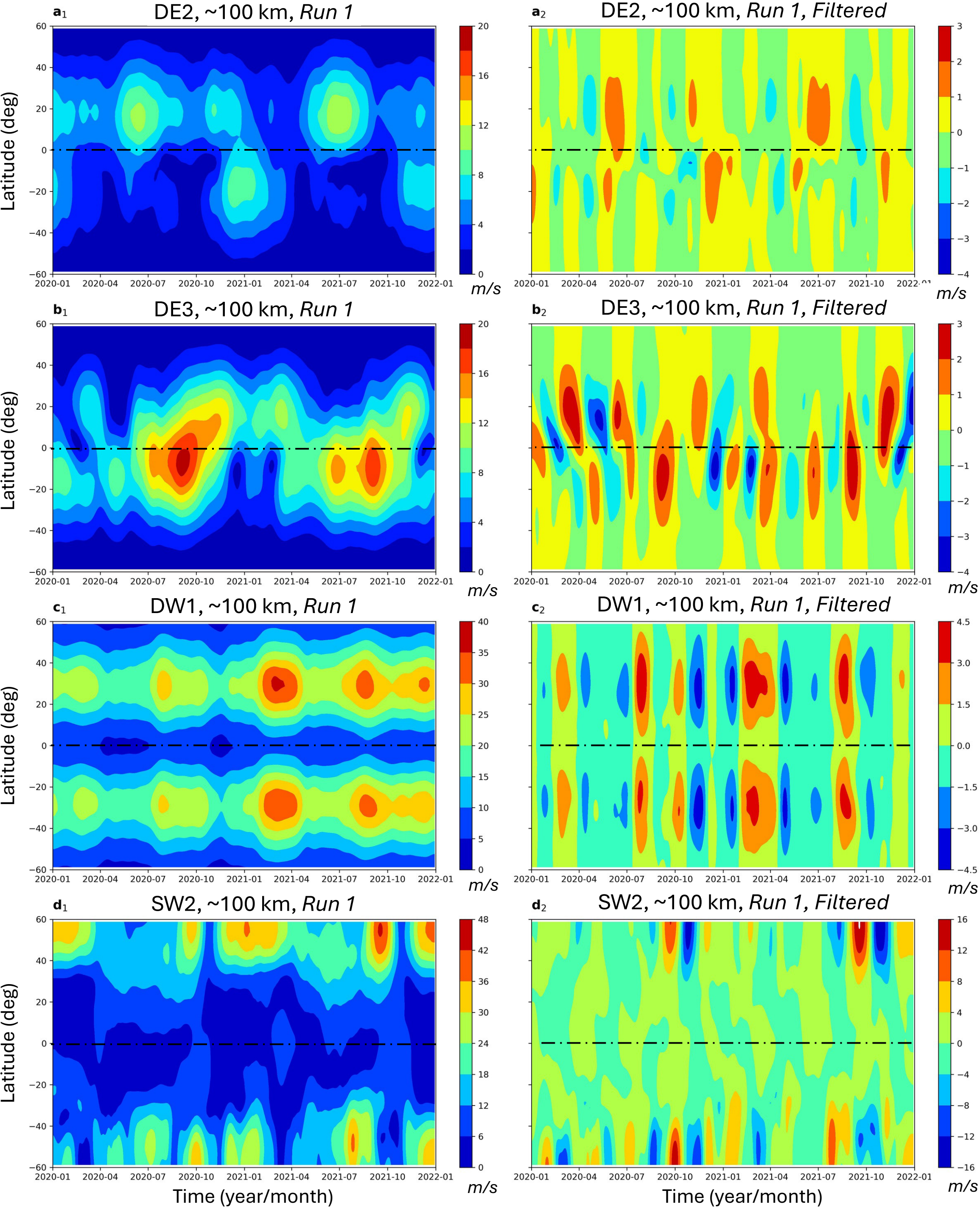

a1 DE2, ~100 km, Run 1
a2 DE2, ~100 km, Run 1, Filtered
b1 DE3, ~100 km, Run 1
b2 DE3, ~100 km, Run 1, Filtered
c1 DW1, ~100 km, Run 1
c2 DW1, ~100 km, Run 1, Filtered
d1 SW2, ~100 km, Run 1
d2 SW2, ~100 km, Run 1, Filtered
Latitude (deg)
Time (year/month)
m/s

Figure 7.

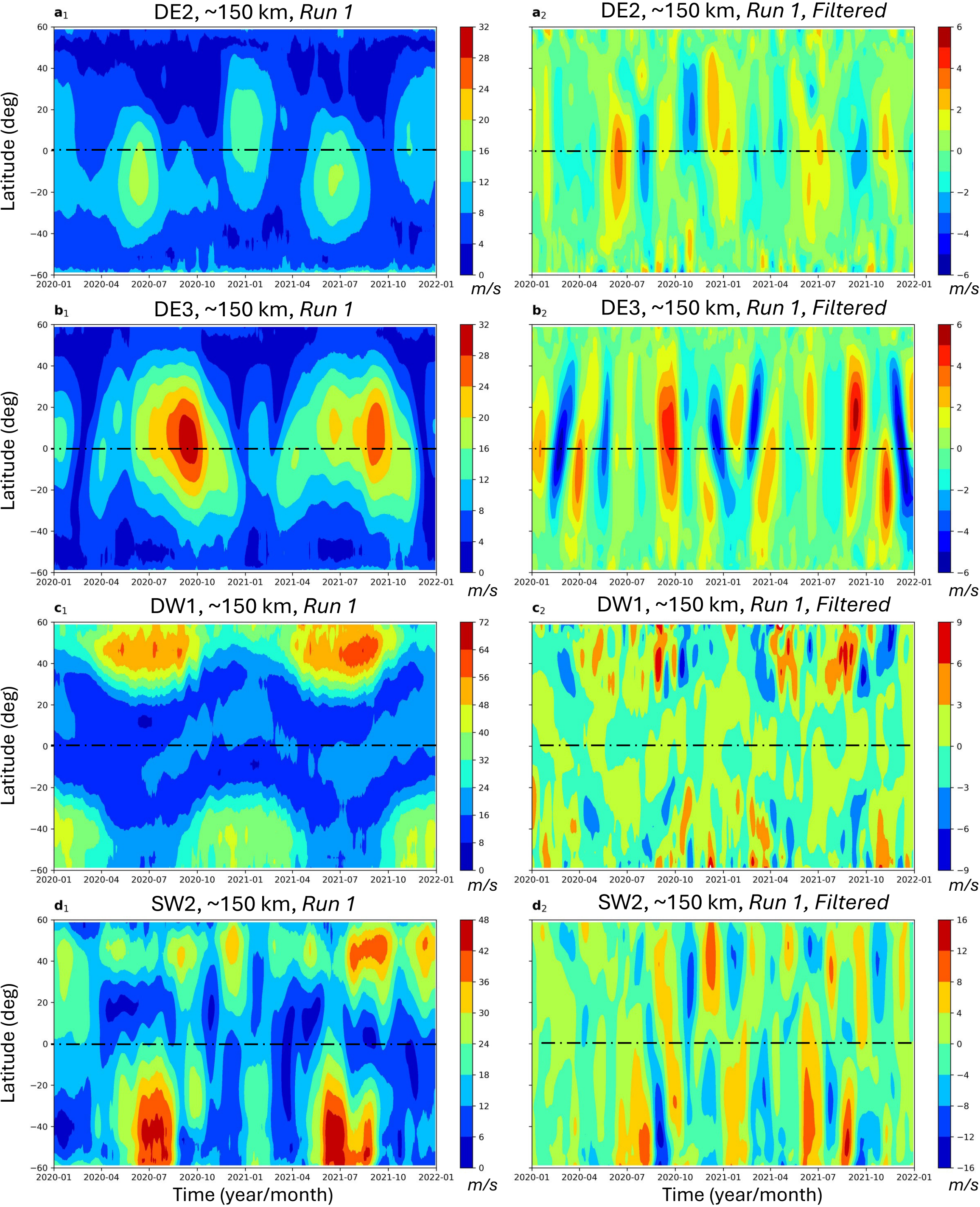
a1 DE2, ~150 km, Run 1
a2 DE2, ~150 km, Run 1, Filtered
b1 DE3, ~150 km, Run 1
b2 DE3, ~150 km, Run 1, Filtered
c1 DW1, ~150 km, Run 1
c2 DW1, ~150 km, Run 1, Filtered
d1 SW2, ~150 km, Run 1
d2 SW2, ~150 km, Run 1, Filtered
Latitude (deg)
Time (year/month)
m/s
2020-01
2020-04
2020-07
2020-10
2021-01
2021-04
2021-07
2021-10
2022-01

Figure 8.

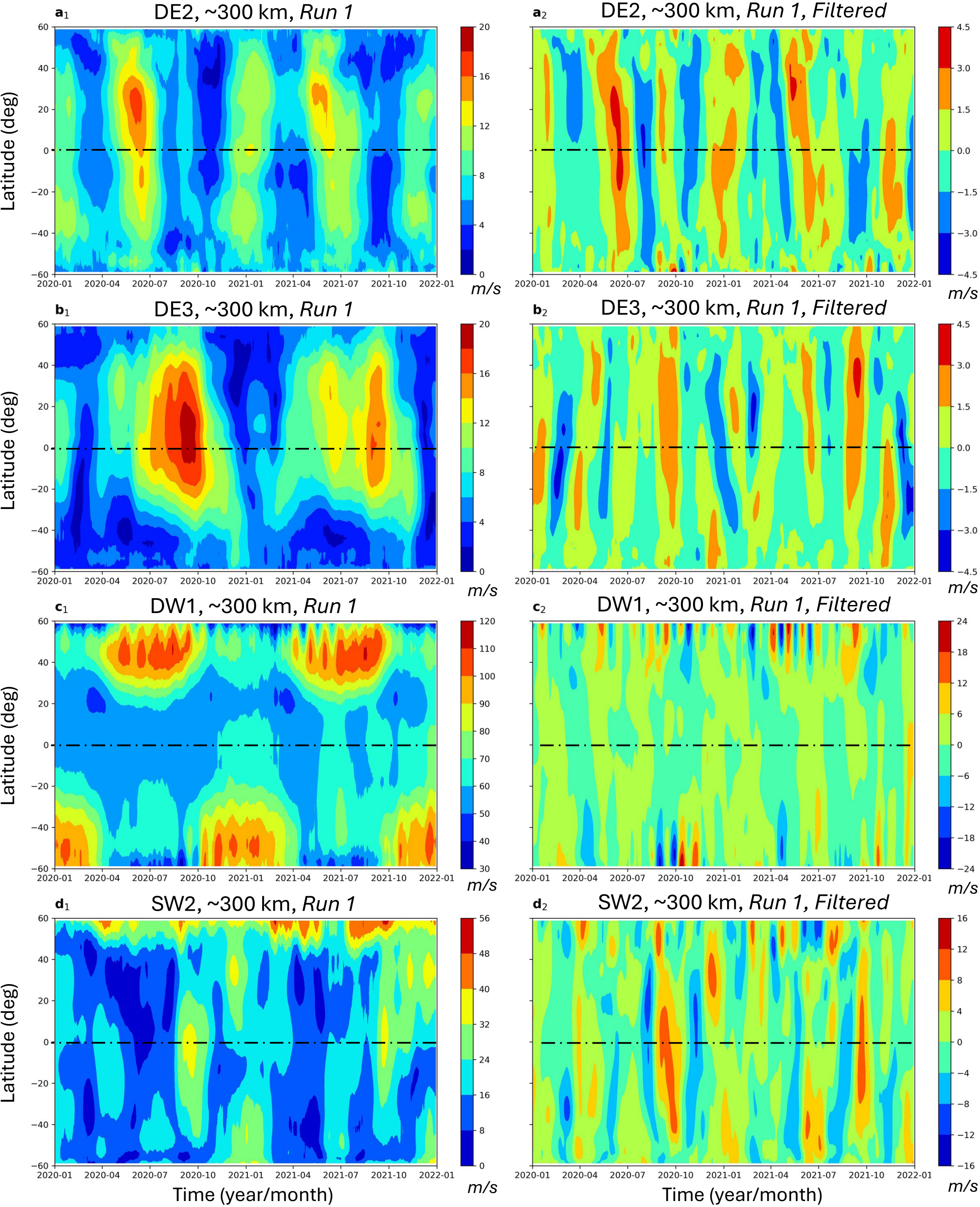

a1 DE2, ~300 km, Run 1
a2 DE2, ~300 km, Run 1, Filtered
b1 DE3, ~300 km, Run 1
b2 DE3, ~300 km, Run 1, Filtered
c1 DW1, ~300 km, Run 1
c2 DW1, ~300 km, Run 1, Filtered
d1 SW2, ~300 km, Run 1
d2 SW2, ~300 km, Run 1, Filtered
Latitude (deg)
Time (year/month)
m/s

Figure 9.

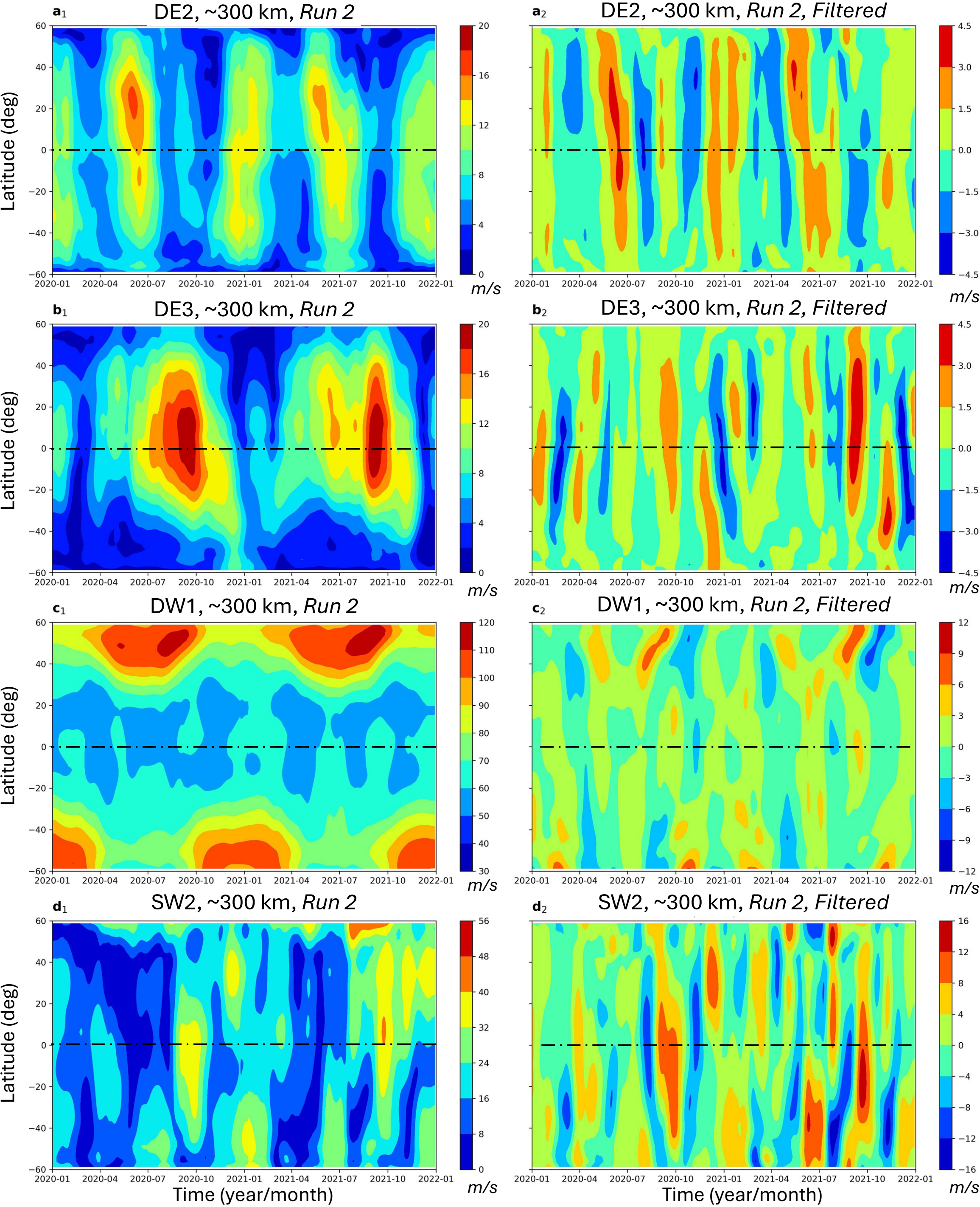

a1
DE2, ~300 km, Run 2
a2
DE2, ~300 km, Run 2, Filtered
b1
DE3, ~300 km, Run 2
b2
DE3, ~300 km, Run 2, Filtered
c1
DW1, ~300 km, Run 2
c2
DW1, ~300 km, Run 2, Filtered
d1
SW2, ~300 km, Run 2
d2
SW2, ~300 km, Run 2, Filtered
Latitude (deg)
Time (year/month)
m/s
2020-01
2020-04
2020-07
2020-10
2021-01
2021-04
2021-07
2021-10
2022-01

Figure 10.

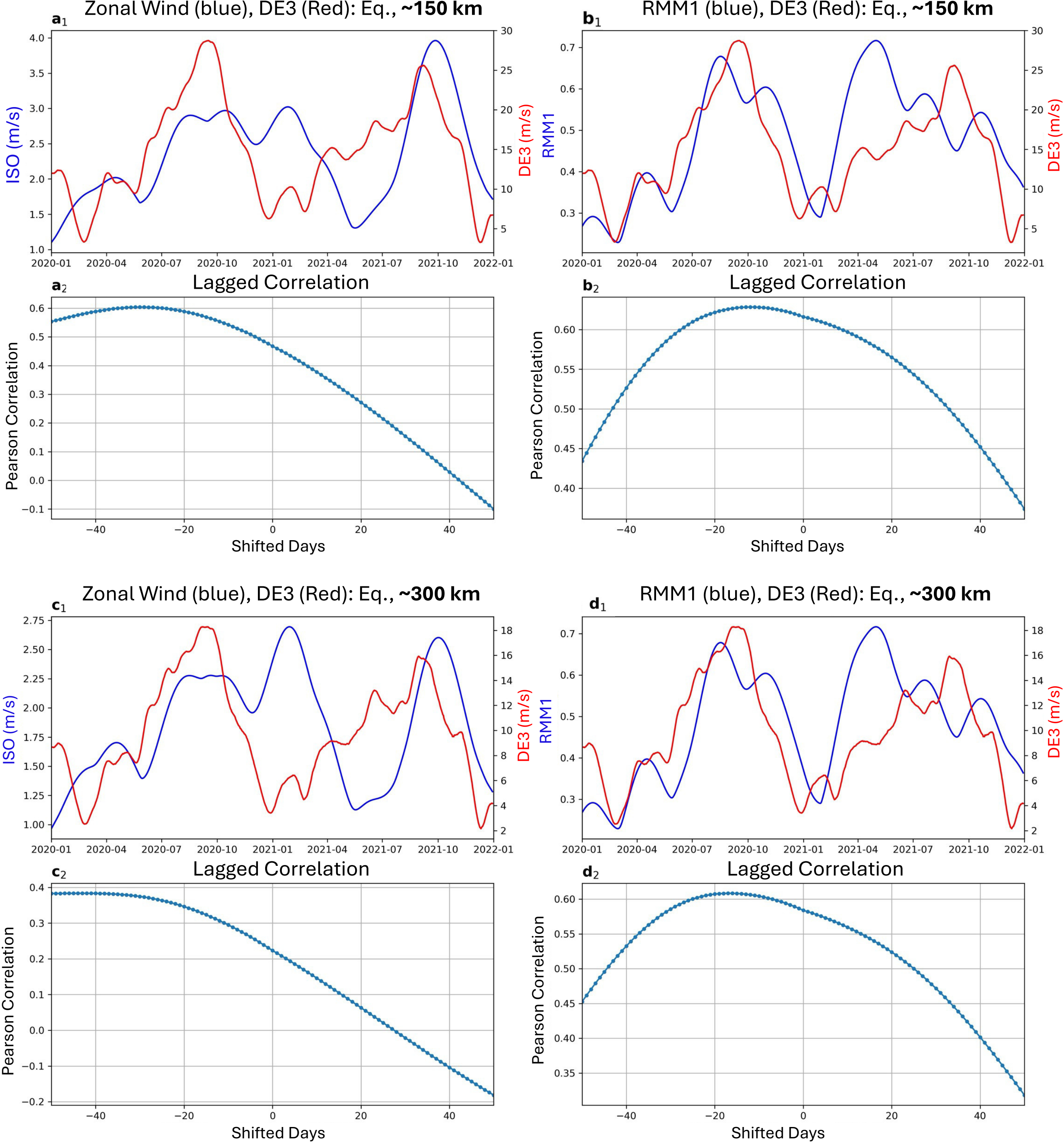

a_1
Zonal Wind (blue), DE3 (Red): Eq., **~150 km**
ISO (m/s)
DE3 (m/s)
1.0
1.5
2.0
2.5
3.0
3.5
4.0
5
10
15
20
25
30
2020-01
2020-04
2020-07
2020-10
2021-01
2021-04
2021-07
2021-10
2022-01
b_1
RMM1 (blue), DE3 (Red): Eq., **~150 km**
RMM1
DE3 (m/s)
0.3
0.4
0.5
0.6
0.7
5
10
15
20
25
30
2020-01
2020-04
2020-07
2020-10
2021-01
2021-04
2021-07
2021-10
2022-01
a_2
Lagged Correlation
Pearson Correlation
−0.1
0.0
0.1
0.2
0.3
0.4
0.5
0.6
−40
−20
0
20
40
Shifted Days
b_2
Lagged Correlation
Pearson Correlation
0.40
0.45
0.50
0.55
0.60
−40
−20
0
20
40
Shifted Days
c_1
Zonal Wind (blue), DE3 (Red): Eq., **~300 km**
ISO (m/s)
DE3 (m/s)
1.00
1.25
1.50
1.75
2.00
2.25
2.50
2.75
2
4
6
8
10
12
14
16
18
2020-01
2020-04
2020-07
2020-10
2021-01
2021-04
2021-07
2021-10
2022-01
d_1
RMM1 (blue), DE3 (Red): Eq., **~300 km**
RMM1
DE3 (m/s)
0.3
0.4
0.5
0.6
0.7
2
4
6
8
10
12
14
16
18
2020-01
2020-04
2020-07
2020-10
2021-01
2021-04
2021-07
2021-10
2022-01
c_2
Lagged Correlation
Pearson Correlation
−0.2
−0.1
0.0
0.1
0.2
0.3
0.4
−40
−20
0
20
40
Shifted Days
d_2
Lagged Correlation
Pearson Correlation
0.35
0.40
0.45
0.50
0.55
0.60
−40
−20
0
20
40
Shifted Days

Figure 11.

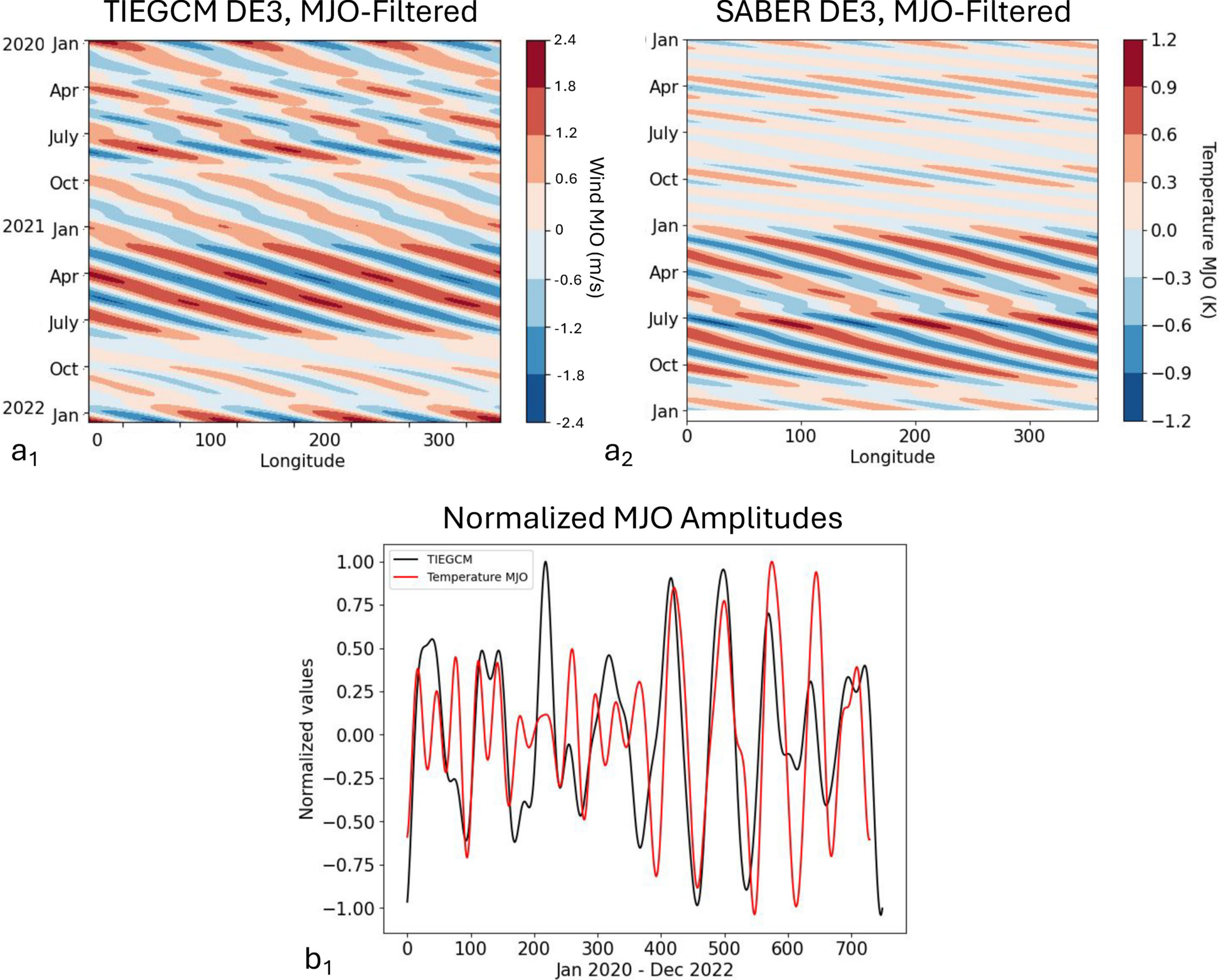
TIEGCM DE3, MJO-Filtered
2020 Jan
Apr
July
Oct
2021 Jan
Apr
July
Oct
2022 Jan
0
100
200
300
Longitude
2.4
1.8
1.2
0.6
0
-0.6
-1.2
-1.8
-2.4
Wind MJO (m/s)
a1
SABER DE3, MJO-Filtered
Jan
Apr
July
Oct
Jan
Apr
July
Oct
Jan
Longitude
1.2
0.9
0.6
0.3
0.0
−0.3
−0.6
−0.9
−1.2
Temperature MJO (K)
a2
Normalized MJO Amplitudes
TIEGCM
Temperature MJO
1.00
0.75
0.50
0.25
0.00
−0.25
−0.50
−0.75
−1.00
Normalized values
0
100
200
300
400
500
600
700
Jan 2020 - Dec 2022
b1